

Omnidirectional spin-to-charge conversion in graphene/NbSe₂ van der Waals heterostructures

Josep Ingla-Aynés,^{1,2,*} Inge Groen,¹ Franz Herling,¹ Nerea Ontoso,¹ C. K. Safeer,¹
 Fernando de Juan,^{3,4} Luis E. Hueso,^{1,4} Marco Gobbi,^{1,4} and Fèlix Casanova^{1,4,†}

¹*CIC nanoGUNE BRTA, 20018 Donostia-San Sebastian, Basque Country, Spain*

²*Current address: Kavli Institute of Nanoscience,*

Delft University of Technology, Lorentzweg 1, Delft 2628 CJ, The Netherlands

³*Donostia International Physics Center (DIPC),*

20018 Donostia-San Sebastian, Basque Country, Spain

⁴*IKERBASQUE, Basque Foundation for Science, 48013 Bilbao, Basque Country, Spain*

(Dated: May 17, 2022)

The conversion of spin currents polarized in different directions into charge currents is a keystone for novel spintronic devices. Van der Waals heterostructures with tailored symmetry are a very appealing platform for such a goal. Here, by performing nonlocal spin precession experiments, we demonstrate the spin-to-charge conversion (SCC) of spins oriented in all three directions (x , y , and z). By analyzing the magnitude and temperature dependence of the signal in different configurations, we argue that the different SCC components measured are likely due to spin-orbit proximity and broken symmetry at the twisted graphene/NbSe₂ interface. Such efficient omnidirectional SCC opens the door to the use of new architectures in spintronic devices, from spin-orbit torques that can switch any magnetization to the magnetic state readout of magnetic elements pointing in any direction.

Keywords: spin-to-charge conversion, van der Waals heterostructures, symmetry

INTRODUCTION

Efficient spin-to-charge conversion (SCC) is a crucial ingredient for spintronics and has been widely studied over the last decade [1]. In conventional materials with high symmetry, a charge current density (j_c) is converted into a spin current density ($j_s \propto j_c \times s$, where s is the spin polarization direction) that is perpendicular to j_c and s via the spin Hall effect (SHE). In two-dimensional systems without structural inversion symmetry, the Edelstein effect (EE) emerges. In this case, an in-plane j_c leads to a perpendicularly polarized spin density (n_s), also in the device plane [2]. Both effects obey reciprocity, implying that the inverse transformations (of j_s and n_s into j_c) also occur with the same efficiency in the linear response regime [1]. While the SHE has been used to switch [3, 4] and probe [5, 6] the magnetization of adjacent ferromagnets, the integration of spintronic devices into logic circuits still requires the introduction of materials with better SCC efficiency. Furthermore, the search for new spin manipulation approaches requires versatile materials that allow SCC of spins polarized along different directions, a feature that is not achievable in conventional materials.

In this context, layered materials emerge as a versatile platform for efficient SCC [7–19] that induces large spin-orbit torques (SOTs) in different directions [20, 21] that can switch the magnetization of adjacent ferromagnets [22–24]. In particular, additional SCC components emerge in layered materials with reduced symmetry, such as 1T'-MoTe₂ [25, 26] and Td-WTe₂ [20]. In van der Waals heterostructures where these materials are com-

bined with graphene, an additional SCC component has also been observed with s parallel to the generated j_c [27, 28]. Because this component is incompatible with the bulk symmetries of MoTe₂ and WTe₂, its origin remains elusive [27].

Additionally, SOTs measured in NbSe₂/Py bilayers have also shown the presence of an additional component not allowed by symmetry, that is sample-dependent and induced by out-of-plane spins parallel to j_s [21]. This SCC component is not allowed due to the two mirror symmetries of bulk 2H-NbSe₂. These symmetries only enable the conversion of spins which are perpendicular to both j_s and j_c via the SHE [29–32]. Accordingly, new experiments combining graphene and van der Waals materials with high spin-orbit coupling (SOC) are required to understand the origin of the unexpected components. Furthermore, efficient conversions are expected from first-principles calculations, that have extracted spin-orbit proximities up to 40 meV in graphene/NbSe₂ heterostructures [33], further motivating these experiments. Finally, even though unconventional SCC components have been observed, the achievement of omnidirectional SCC in a single device has not been realized yet.

Here, we perform nonlocal spin precession experiments to investigate SCC in graphene/NbSe₂ van der Waals heterostructures (Fig. 1a). Our experiments show that all three spin directions (x , y , and z) are converted into a charge current simultaneously while keeping the j_c direction fixed (see Fig. 1b) and constitute the first realization of omnidirectional SCC. Quantitative data analysis indicates that the effects originate from at least three differ-

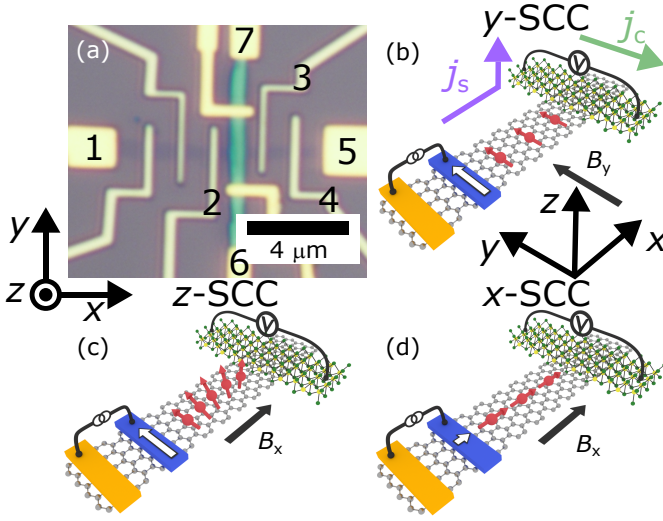


FIG. 1. Device geometry implemented to detect the omnidirectional spin-to-charge conversion. (a) Optical microscope image of sample 1. The green vertical stripe is the NbSe₂ flake and is contacted by four Ti/Au contacts. The graphene is the dark horizontal stripe and is contacted by TiO_x/Co electrodes (vertically oriented) and by two bigger Ti/Au contacts at the ends. (b-d) Sketches of the SCC measurement configurations used here. In b, the magnetic field is swept along the easy axis of the Co electrode, leading to magnetization switching, that reverses the sign of the y -SCC signal. The spin current density (j_s) and the converted charge current density (j_c) directions are also shown. Note that j_s can also have an x -component in the NbSe₂ and proximitized graphene regions. In c, a small magnetic field applied along x leads to out-of-plane spin precession, enabling the measurement of z -SCC. In d, by increasing the magnetic field further, the Co magnetization is saturated, leading to the measurement of x -SCC.

ent SCC phenomena stemming from the SOC of NbSe₂, its proximity with graphene and the broken symmetry at the twisted graphene/NbSe₂ interface.

EXPERIMENTAL DETAILS

The graphene and NbSe₂ flakes were prepared using the conventional mechanical exfoliation technique [34] from highly oriented pyrolytic graphite and bulk NbSe₂ provided by HQ Graphene. The heterostructure was prepared using the PDMS-based viscoelastic transfer technique [35] in an inert atmosphere. The Ti (5 nm)/Au (120 nm) and spin-polarized TiO_x (0.3 nm)/Co (35 nm) electrodes were defined using e-beam lithography and deposited using e-beam and thermal evaporation (see Supplementary Information section S1). An optical microscope image of sample 1 after fabrication is shown in Fig. 1a, where the used electrodes are numbered. The results shown here are obtained from sample 1, see the Supplementary Information section S9 for sample 2. To optimize and keep the spin transport properties of the

graphene channel nearly constant with the temperature, we have tuned the carrier density far from the charge neutrality point using a backgate voltage [34]. No SCC signals have been measured near the charge neutrality point (see Supplementary Information section S2, S3, S6 and S9 for details on the V_{bg} dependence of charge and spin transport in graphene and SCC in sample 2). Additionally, to minimize background effects and exclude even harmonics from our measurements, we have used the DC reversal technique with an applied current of 60 μ A.

RESULTS

To measure SCC, we use the nonlocal measurement technique, that avoids spurious effects related to local techniques such as the Oersted fields present in SOT experiments [36] and the voltages induced by stray fields measured in potentiometric measurements [37, 38]. By applying a charge current (I) between electrodes 3 and 5, we inject a spin-polarized current in the graphene channel under electrode 3, leading to a pure spin current that diffuses to the NbSe₂-covered region, where it can get converted into a j_c via SCC in the proximitized graphene and/or absorbed by the NbSe₂ flake in which the SCC can subsequently occur. The j_c induced by SCC is detected as an open circuit voltage V between the non-magnetic contacts 7 and 6, giving rise to a nonlocal signal $R_{nl} = V/I$. Due to shape anisotropy, the easy axis of our Co electrodes is along y . Hence, the application of magnetic field (B) of more than 50 mT along $\pm y$ leads to the alignment of the electrode magnetization (Fig. 1b). By preparing the magnetization of electrode 3 (M_3) along $+y \equiv \uparrow$ or along $-y \equiv \downarrow$ and applying B along $\pm x$ (B_x , see Figs. 1c and 1d), we obtain the nonlocal signals R_{nl}^\uparrow and R_{nl}^\downarrow , respectively, which are shown in Fig. 2a. To separate between the different SCC components, we define $R_{SCC} = (R_{nl}^\uparrow - R_{nl}^\downarrow)/2$ (Fig. 2b), which contains the y - and z -SCC signals, and $R_{avg} = (R_{nl}^\uparrow + R_{nl}^\downarrow)/2$ (Fig. 2f), which corresponds to x -SCC. Here, to simplify our notation, we refer to each SCC component as x , y or z -SCC depending only on the spin direction.

First, we focus on the y - and z -SCC components. When B_x is applied, the injected spins start to precess in the y - z plane, leading to a net out-of-plane spin accumulation (μ_{sz} , see Fig. 1c). Because reversing the sign of B_x leads to opposite μ_{sz} , the R_{nl} expected from the z -SCC is antisymmetric with respect to B_x . Additionally, switching (the y component of) M_3 also leads to a sign change of the signal. Accordingly, to extract the z -SCC component, we have calculated the antisymmetric component of R_{SCC} (R_{SCC}^{anti}) as a function of B_x . The results from Fig. 2c confirm that z -spins are converted in our system, giving rise to a maximum R_{SCC}^{anti} of 0.13 ± 0.02 m Ω . We note that R_{SCC} also contains a clear symmetric compo-

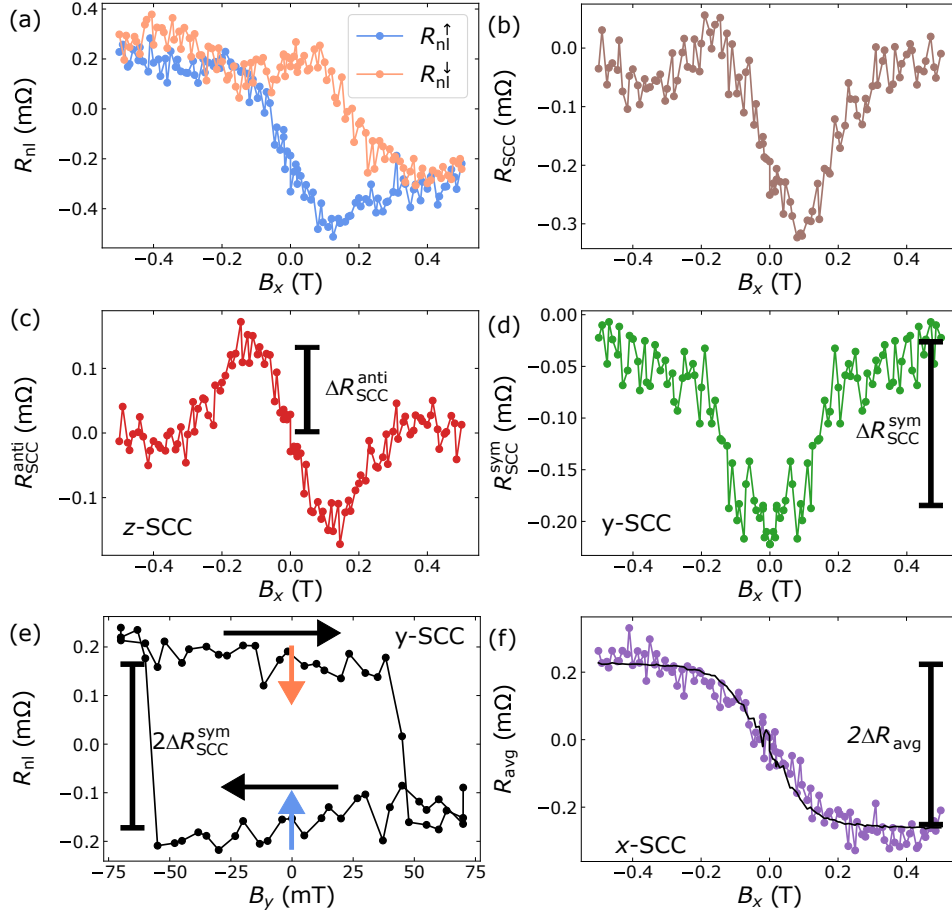


FIG. 2. Nonlocal spin-to-charge conversion at 100 K and $V_{bg}=50$ V. (a) R_{nl} as a function of B_x measured at the \uparrow and \downarrow magnetization configurations. (b) $R_{SCC} = (R_{nl}^{\uparrow} - R_{nl}^{\downarrow})/2$ extracted from panel a. (c) Antisymmetric component of R_{SCC} vs B_x corresponding to z -SCC with its associated amplitude ΔR_{SCC}^{anti} . (d) Symmetric component of R_{SCC} vs B_x corresponding to y -SCC with its associated amplitude ΔR_{SCC}^{sym} . (e) R_{nl} as a function of B_y . The jumps in R_{nl} correspond to switches of the injector magnetization originated from y -SCC. (f) $R_{avg} = (R_{nl}^{\uparrow} + R_{nl}^{\downarrow})/2$ extracted from panel a with its associated amplitude ΔR_{avg} . The black line corresponds to the magnetization behaviour extracted from the reference Hanle precession data. An offset of 1.85 mΩ has been subtracted from panels a and e.

ment with B_x (R_{SCC}^{sym}). This component, which is shown in Fig. 2d, might correspond to a conventional Hanle spin precession measurement, that is induced by a y -SCC component. Since the detected spins are parallel to the injected ones, the resulting R_{SCC} decreases as the spins precess towards $\pm z$ and the y -spin-projection decreases symmetrically with B_x . We realize that B_x also induces the pulling of M_3 along x , leading to a decrease of the signal as $|B_x|$ increases. Because of the short spin lifetime of our graphene channel (see Supplementary Information section S3), we find that the lineshape is actually dominated by contact pulling, and not by spin precession. We finally note that the apparently flat trend of Fig. 2d near $B_x = 0$, that is not expected from Hanle spin precession, is caused by the symmetrization of the noise in R_{SCC} . We note that the y -SCC component is not expected from 2H-NbSe₂ and, to confirm that this SCC component is indeed present in our sample, we apply a magnetic field along

y (B_y) to control the electrode magnetization. When M_3 switches, the y -SCC signal reverses sign, allowing us to extract the signal magnitude (Fig. 1b). In Fig. 2e, we show the B_y -dependence of R_{nl} . When sweeping B_y from -75 to $+75$ mT, we observe a clear jump in R_{nl} for $B_y \equiv B_y^{sw} = 50$ mT, which is caused by the switch of M_3 . Additionally, sweeping B_y from $+75$ to -75 mT leads to a jump in R_{nl} at $B_y \approx -B_y^{sw}$, as expected for the switching of M_3 in the opposite direction. Note that, because $R_{SCC} = (R_{nl}^{\uparrow} - R_{nl}^{\downarrow})/2$, the spin signal in Fig. 2d should be approximately one half of the 0.34 ± 0.03 mΩ extracted from Fig. 2e. In agreement, we observe that the signal in Fig. 2d is of 0.16 ± 0.02 mΩ. Both signals are determined for $B = 0$.

As B_x increases, M_3 gets pulled towards x , leading to the injection of x -spins (Fig. 1d). Unlike the previous spin injection components, x -SCC does not depend on the initial orientation of M_3 in the y axis. Hence, we

isolate x -SCC by determining R_{avg} . As shown in Fig. 2f, purple dots, the signal is antisymmetric and saturates at $R_{\text{avg}} = 0.27 \pm 0.06 \text{ m}\Omega$ for $|B_x| > 0.2 \text{ T}$, as expected from the contact magnetization behaviour [39]. To compare R_{avg} with the x -component of M_3 ($M_3 \sin(\theta_M)$, where θ_M is the magnetization angle with respect to the easy axis) extracted from spin precession in the pristine graphene region (see Supplementary Information section S3), we have re-scaled $\sin(\theta_M)$ and plotted it as a black line in Fig. 2f. The overlap between both curves confirms that R_{avg} follows $\sin(\theta_M)$. However, the conventional Hall effect in the graphene channel induced by the stray fields from the ferromagnetic spin injector can also lead to similar signals [9, 40]. To confirm that R_{avg} is induced by SCC, we have measured R_{SCC} in sample 2 as a function of an out-of-plane magnetic field to induce in-plane spin precession, an unequivocal proof for spin transport (see Supplementary Information section S9).

Finally, to compare between the different signals, in Fig. 2 we define the signal amplitudes ΔR_{avg} , $\Delta R_{\text{SCC}}^{\text{sym}}$ and $\Delta R_{\text{SCC}}^{\text{anti}}$ as the semi-difference between the maximum and minimum signal vs B_x .

To further understand the measured SCC, we study the temperature (T) dependence of ΔR_{avg} , $\Delta R_{\text{SCC}}^{\text{sym}}$ and $\Delta R_{\text{SCC}}^{\text{anti}}$, corresponding to x , y and z -SCC, respectively. In Fig. 3a, we observe that ΔR_{avg} and $\Delta R_{\text{SCC}}^{\text{sym}}$ increase with T (with the exception of ΔR_{avg} at 300 K), in contrast with $\Delta R_{\text{SCC}}^{\text{anti}}$, that shows a maximum at 100 K and decreases for higher T (see Supplementary Information section S4 for the complete dataset and S5 for the reciprocity experiments that confirm that our work is in the linear response regime).

DISCUSSION

After showing that x -, y -, and z -SCC occur simultaneously by spin precession measurements and how the resulting signals evolve with T , now we proceed to discuss the origin of the different SCC components.

For this purpose, and because shunting prevents the accurate determination of the relevant transport parameters of proximitized graphene, we estimate the lower bound of the absolute value of the x -, y -, and z -SCC-associated spin Hall angles ($(|\theta_{ij}^k|)_{\text{min}}$, where i , j , and k are the directions of j_s , j_c and s , respectively) assuming that the SCC occurs in the NbSe₂ flake (see Supplementary Information section S8 for details). The results from our analysis are shown in Fig. 3b as a function of T . We observe that the error range (shaded areas) increases dramatically upon cooling below 100 K. This effect is caused by the decrease in ρ_{NbSe_2} (that is assumed to be isotropic) shown in the inset. The decrease in the device resistance with decreasing T leads to much smaller signals while keeping $(|\theta_{ij}^k|)_{\text{min}}$ constant, decreasing the sensitivity of our measurement below 100 K. We stress that the result-

ing $(|\theta_{ij}^k|)_{\text{min}}$ values are only valid under the assumption that the conversion occurs in the NbSe₂ flake. If the SCC occurs in the proximitized graphene, lower efficiencies are to be expected.

First, we discuss the z -SCC component. It can be caused by the inverse SHE in proximitized graphene [8, 10, 13, 14] (Fig. 4c), by the conventional inverse SHE in NbSe₂ due to a spin current polarized along z and diffusing along x (Fig. 4f light red and blue spins), or due to the unconventional out-of-plane SCC component in NbSe₂ (Fig. 4f red and blue spins) reported in Ref. [21]. The z -SCC origin can be discerned by changing the sign of j_s in the graphene channel (along x -axis). If the SCC occurs in the proximitized graphene channel or by conventional SHE in NbSe₂, because the relevant j_s flows along x , R_{SCC} must change sign with j_s . In contrast, if the SCC occurs via unconventional out-of-plane SCC in the NbSe₂ flake, because the relevant j_s points along z in the NbSe₂, the sign of R_{SCC} should not change when changing the in-plane j_s direction. To discern between these effects, we compare between R_{nl} obtained using electrodes 3 and 2 to inject spins (Fig. 4g). The results are shown in Figs. 4h and 4i, respectively. We observe that $R_{\text{SCC}}^{\text{sym}}$ and R_{avg} do not change sign when changing the spin injector (i.e. the in-plane j_s direction) but $R_{\text{SCC}}^{\text{anti}}$ does, indicating that the z -SCC is induced by the inverse SHE in the proximitized graphene channel or the NbSe₂ flake. Now we need to discern between both possibilities. Looking at the spin Hall angle, we note that $|\theta_{xy}^z|$ is higher than 50% at 100 K. The quantification performed here assumes that j_s is absorbed all along z in the NbSe₂. Because the x -component of j_s in NbSe₂ is smaller than the total j_s , the red line in Fig. 3b provides an even lower bound to $|\theta_{xy}^z|$ and the true spin Hall angle is expected to be higher. In this context, since 50% is already significantly larger than observed previously in NbSe₂ devices[21], it is safe to assume that the z -SCC component originates from the proximitized graphene layer instead of the NbSe₂. Due to shunting by the NbSe₂, we cannot obtain the charge and spin transport parameters of the proximitized graphene region. Since these parameters are required to quantify the proximity-induced SCC efficiency, the subsequent quantitative analysis (Fig. 3c) assuming that the SCC occurs in the NbSe₂ channel is not performed for the z -SCC component.

Next, we address the in-plane SCC components. x -SCC can be induced by both the conventional EE in the proximitized graphene (Fig. 4a) and the conventional SHE in NbSe₂ (Fig. 4d). The lack of a sign reversal of the x -SCC component when reversing the spin current direction (Fig. 4g-i) is consistent with both possibilities. As a consequence, we cannot discern between them by symmetry considerations. In bulk NbSe₂, the y -SCC component should in principle be forbidden by symmetry [21]. However, at the first NbSe₂ layer, which has C_{3v} symmetry, there is an allowed SHE component

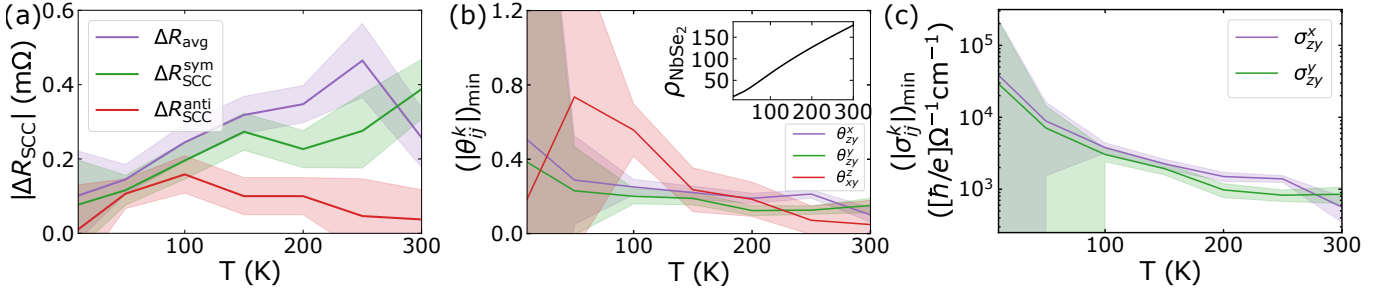


FIG. 3. Temperature dependence of (a) the spin-to-charge conversion signal amplitude ($|\Delta R_{SCC}|$) at $V_{bg} = 50$ V and the lower bound of (b) the spin Hall angle ($|\theta_{ij}^k|$), and (c) the spin Hall conductivity ($|\sigma_{ij}^k|$). The inset of panel b shows the resistivity of NbSe₂ in $\mu\Omega cm$ as a function of temperature. The shaded areas correspond to the experimental uncertainty ranges.

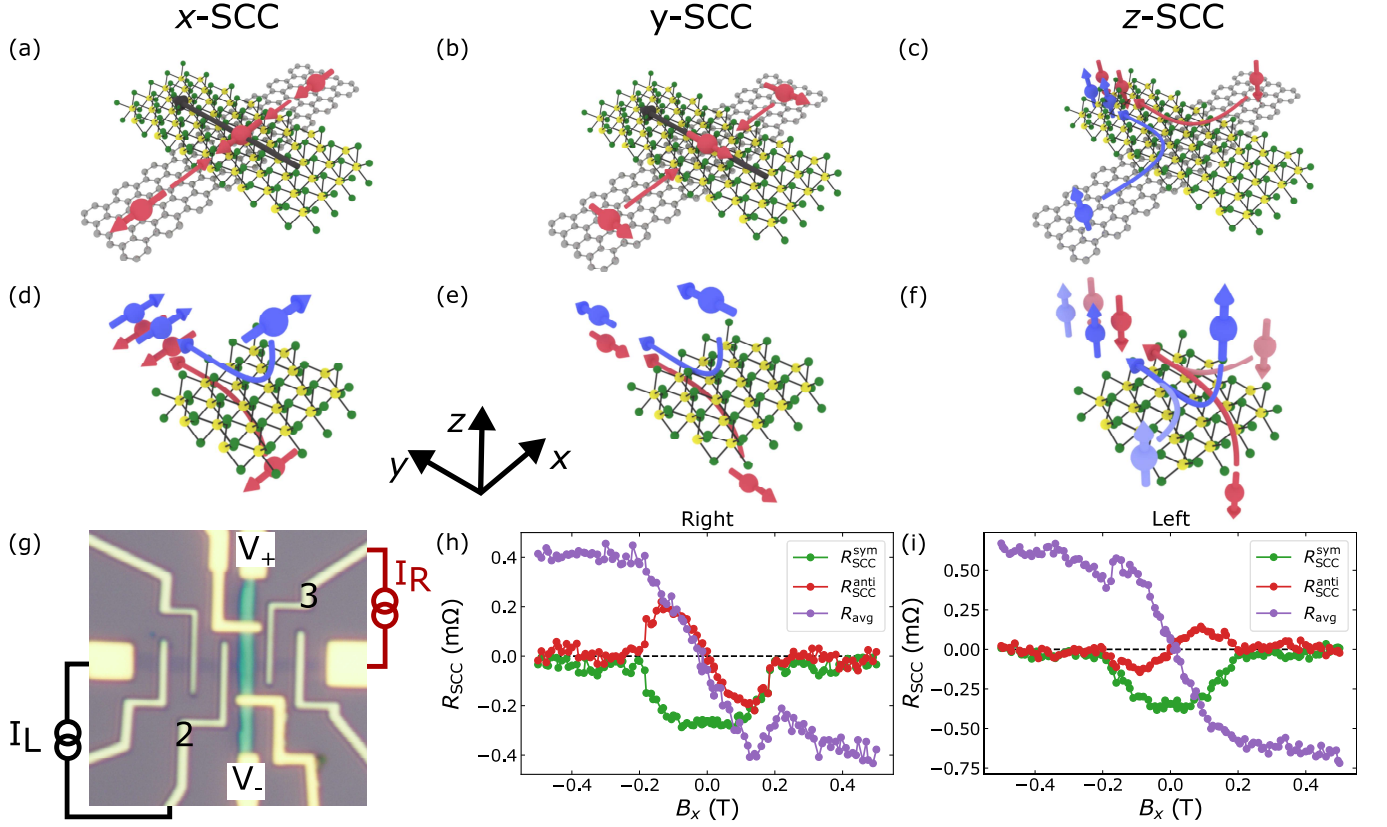


FIG. 4. (a)-(c) Proximity-induced SCC in graphene/NbSe₂ heterostructures. Conventional (a) and unconventional (b) inverse EE in proximitized graphene lead to the conversion of x - and y -spins, respectively, into a y -charge current. (c) Inverse SHE in proximitized graphene leads to z -SCC. (d)-(f) Possible SHE components originating in the NbSe₂ flake. (d) A spin current polarized along x and propagating along z gives rise to a charge current along y via the conventional inverse SHE. (e) Under shear strain, a spin current polarized along y and propagating along z can give rise to a y -charge current in NbSe₂. (f) A spin current polarized along z and propagating along z and x can give rise to a y -charge current via unconventional and conventional (inverse) SHE, respectively. (g) SCC is measured at 100 K and $V_{bg} = 70$ V using a spin current source placed at the right (I_R) (h) and left (I_L) (i) sides of the NbSe₂ flake. An offset of 2.3 and 1.5 m Ω has been subtracted from R_{avg} in panels (h) and (i), respectively.

that would convert y -spins propagating along x into a charge current along y [29–32]. However, the lack of a sign reversal of the y -SCC component when reversing the spin current direction (Fig. 4g-i) rules out this possibility.

Additionally, we note that for any twist angle between the crystal mirrors of the NbSe₂ and graphene flakes that is not a multiple of 30 degrees, the graphene and NbSe₂ vertical mirrors are not aligned, so that neither

can be a mirror for the whole structure, resulting in a C_3 point group that does not have any mirror symmetry, enabling y -SCC via unconventional EE in the proximitized graphene [41, 42] as shown in Fig. 4b (see Supplementary Information section S11 for a detailed symmetry discussion). Furthermore, recent first-principles calculations on twisted graphene/transition metal dichalcogenide heterostructures [43, 44] have shown that the radial component of the in-plane SOC can have a similar magnitude as the conventional Rashba SOC component [43] depending on the electric field and twist angle, indicating that the measured component is likely to arise from the EE in the graphene channel. Finally, shear strain could also break enough symmetries in the NbSe₂ flake, enabling a SCC component where y -polarized spins flow in the z direction in NbSe₂ (Fig. 4e) and propagate into the graphene channel [27]. The lack of a sign change of $R_{\text{SCC}}^{\text{sym}}$ when reversing the spin current direction (Fig. 4g-i) is compatible with the two mentioned mechanisms.

To gain insight into the origin of the in-plane SCC components, we discuss the $(|\theta_{ij}^k|)_{\min}$ shown in Fig. 3b that assumes that the SCC occurs in the NbSe₂ flake. We observe that, at 100 K, in-plane $(|\theta_{ij}^k|)_{\min}$ reaches the highest value, which is 25 and 20% for x - and y -SCC, respectively. At higher T , the measured signals increase, leading to minimum $(|\theta_{ij}^k|)_{\min}$ values of 10 and 15% at 300 K for spins polarized along x and y , respectively.

We can compare our results with SOT experiments by calculating the spin Hall conductivity $(\sigma_{ij}^k)_{\min} = (|\theta_{ij}^k|)_{\min}/\rho_{\text{NbSe}_2}$. We find that, at 300 K, $\sigma_{zy}^x = 560 \pm 200$ and $\sigma_{zy}^y = 850 \pm 200$ [\hbar/e] $\Omega^{-1}\text{cm}^{-1}$. These values, which are already large at 300 K, increase an order of magnitude upon cooling to 100 K. Note that the extracted σ_{ij}^k are one order of magnitude larger than the conductivities of up to 75 [\hbar/e](Ωcm)⁻¹ extracted from SOT experiments [21]. The large difference between our results and those of Ref. 21 suggests that both in-plane SCC components, that have similar magnitude, occur in the proximitized graphene layer. Note that, in this case, the injected spins can be converted without overcoming the interface resistance with the NbSe₂ flake (see Supplementary Information section S7 for the determination of the interface resistance). Accordingly, the conversion efficiency required to explain the measured signals is expected to decrease significantly. Furthermore, the reproducible observation of the unconventional y -SCC component in graphene-based heterostructures containing different layered metals (Refs. 27 and 28) suggests that breaking of the symmetry at the interface is the most plausible source for such a conversion. Since the strain has been shown to fluctuate randomly in graphene-based van der Waals heterostructures [45, 46], the consistent occurrence of shear strain in all the devices seems less likely than an imperfect alignment effect. It is also worth noting that, unlike the case of graphene/semiconducting transition metal

dichalcogenide devices, the samples mentioned here are not annealed at high temperatures, minimizing the probability of crystallographic alignment between the different materials [47]. Despite not having an annealing step, we have found that the interface resistances between the graphene and NbSe₂ flakes are lower than 200 Ω in the reported devices, demonstrating that the interface is transparent enough to induce proximity on the graphene flake (see Supplementary Information section S7 for details). For all these reasons, we believe that the signal quantification in Figs. 3b and 3c most likely does not reflect the actual SCC efficiency in our device. However, it shows that proximitized graphene allowed us to measure larger SCC signals than bulk NbSe₂ alone.

To infer whether the twist angle between the graphene and NbSe₂ flakes is a multiple of 30°, an alignment that would be incompatible with our interpretation, we have assumed that the straight edges of the flakes correspond to crystallographic directions and used the optical microscope images to estimate the twist angle between the graphene and NbSe₂ flakes in sample 1. The result is $89^\circ \pm 0.6^\circ$ (see Supplementary Information section S10) and, even though this angle is rather small (it is only 1° from a high-symmetry point), first-principles calculations predict that the radial component of the spin texture depends more strongly on band alignments and electric fields than on the twist angle [43]. As a consequence, we believe that the small twist angle does not contradict the broken-symmetry interpretation.

Finally, we argue that the T -dependence of the SCC signal is consistent with our interpretation. Even though the x - and y -SCC signals increase with T , in contrast with the EE in graphene proximitized by a semiconductor [9], this different behavior can be attributed to the role of NbSe₂ as a shunting layer. As shown in the inset of Fig. 3b, ρ_{NbSe_2} increases dramatically with T , reducing the shunting and thus increasing the SCC signal. In contrast, the z -SCC component decreases when increasing T . Theoretically, it has been predicted that the SHE in proximitized graphene depends on the intervalley scattering time [48–50]. In this context, the metallic NbSe₂ flake may induce extra intervalley scattering and have a detrimental effect on the z -SCC signal at high T .

SUMMARY

In summary, we have shown that graphene/NbSe₂ van der Waals heterostructures convert x , y , and z spins simultaneously. By analyzing the magnitude, T -dependence and symmetry of the SCC signals, we argue that the three components are likely to occur at the NbSe₂-proximitized graphene. In particular, the z -SCC component most likely arises due to SHE, the x -component due to the EE, and the y -SCC component due to unconventional EE at the twisted graphene/NbSe₂

heterostructure. A twist angle between the flakes can break all the mirror symmetries and enable the unconventional EE component. Our discovery of omnidirectional SCC paves the way for novel spintronic devices that use the three spin directions to realize complex operations. For instance, spins in different directions can be controlled independently via SOC-induced spin precession [51] and contribute to the output signal, enabling the realization of new spin-based operations.

ACKNOWLEDGMENTS

We acknowledge R. Llopis and R. Gay for technical assistance. This work is supported by the Spanish MICINN under projects RTI2018-094861-B-I00, PID2019-108153GA-I00 and the Maria de Maeztu Units of Excellence Programme (MDM-2016-0618 and CEX2020-001038-M), by the “Valleytronics” Intel Science Technology Center, and by the European Union H2020 under the Marie Skłodowska-Curie Actions (0766025-QuESTech). J.I.-A. acknowledges postdoctoral fellowship support from the “Juan de la Cierva - Formación” program by the Spanish MICINN (Grant No. FJC2018-038688-I). N.O. thanks the Spanish MICINN for a Ph.D. fellowship (Grant no. BES-2017-07963). C.K.S. acknowledges support from the European Commission for a Marie Skłodowska-Curie individual fellowship (Grant No. 794982-2DSTOP). F. J. acknowledges funding from the Spanish MCI/AEI/FEDER through grant PGC2018-101988-B-C21 and from the Basque government through PIBA grant 2019-81. M.G. acknowledges support from la Caixa Foundation for a Junior Leader fellowship (Grant No. LCF/BQ/PI19/11690017).

* j.ingla@nanogune.eu

† f.casanova@nanogune.eu

- [1] J. Sinova, S. O. Valenzuela, J. Wunderlich, C. Back, and T. Jungwirth, Spin hall effects, *Reviews of Modern Physics* **87**, 1213 (2015).
- [2] A. Manchon, H. C. Koo, J. Nitta, S. Frolov, and R. Duine, New perspectives for rashba spin-orbit coupling, *Nature Materials* **14**, 871 (2015).
- [3] I. M. Miron, K. Garello, G. Gaudin, P.-J. Zermatten, M. V. Costache, S. Auffret, S. Bandiera, B. Rodmacq, A. Schuhl, and P. Gambardella, Perpendicular switching of a single ferromagnetic layer induced by in-plane current injection, *Nature* **476**, 189 (2011).
- [4] L. Liu, C.-F. Pai, Y. Li, H. Tseng, D. Ralph, and R. Buhrman, Spin-torque switching with the giant spin Hall effect of tantalum, *Science* **336**, 555 (2012).
- [5] S. Manipatruni, D. E. Nikonov, C.-C. Lin, T. A. Gosavi, H. Liu, B. Prasad, Y.-L. Huang, E. Bonturim, R. Ramesh, and I. A. Young, Scalable energy-efficient magnetoelectric spin-orbit logic, *Nature* **565**, 35 (2019).
- [6] V. T. Pham, I. Groen, S. Manipatruni, W. Y. Choi, D. E. Nikonov, E. Sagasta, C.-C. Lin, T. A. Gosavi, A. Marty, L. E. Hueso, I. A. Young, *et al.*, Spin-orbit magnetic state readout in scaled ferromagnetic/heavy metal nanostructures, *Nature Electronics* **3**, 309 (2020).
- [7] J. F. Sierra, J. Fabian, R. K. Kawakami, S. Roche, and S. O. Valenzuela, Van der Waals heterostructures for spintronics and opto-spintronics, *Nature Nanotechnology* **16**, 856 (2021).
- [8] C. Safeer, J. Ingla-Aynés, F. Herling, J. H. Garcia, M. Vila, N. Ontoso, M. R. Calvo, S. Roche, L. E. Hueso, and F. Casanova, Room-temperature spin Hall effect in graphene/MoS₂ van der Waals heterostructures, *Nano Letters* **19**, 1074 (2019).
- [9] T. S. Ghiasi, A. A. Kaverzin, P. J. Blah, and B. J. van Wees, Charge-to-spin conversion by the Rashba-Edelstein effect in two-dimensional van der Waals heterostructures up to room temperature, *Nano Letters* **19**, 5959 (2019).
- [10] L. A. Benítez, W. S. Torres, J. F. Sierra, M. Timmermans, J. H. Garcia, S. Roche, M. V. Costache, and S. O. Valenzuela, Tunable room-temperature spin galvanic and spin Hall effects in van der Waals heterostructures, *Nature Materials* **19**, 170 (2020).
- [11] L. Li, J. Zhang, G. Myeong, W. Shin, H. Lim, B. Kim, S. Kim, T. Jin, S. Cavill, B. S. Kim, *et al.*, Gate-tunable reversible Rashba-Edelstein effect in a Few-Layer graphene/2H-TaS₂ heterostructure at room temperature, *ACS Nano* **14**, 5251 (2020).
- [12] D. Khokhriakov, A. M. Hoque, B. Karpiak, and S. P. Dash, Gate-tunable spin-galvanic effect in graphene-topological insulator van der Waals heterostructures at room temperature, *Nature Communications* **11**, 3657 (2020).
- [13] F. Herling, C. Safeer, J. Ingla-Aynés, N. Ontoso, L. E. Hueso, and F. Casanova, Gate tunability of highly efficient spin-to-charge conversion by spin Hall effect in graphene proximitized with WSe₂, *APL Materials* **8**, 071103 (2020).
- [14] C. Safeer, J. Ingla-Aynés, N. Ontoso, F. Herling, W. Yan, L. E. Hueso, and F. Casanova, Spin hall effect in bilayer graphene combined with an insulator up to room temperature, *Nano Letters* **20**, 4573 (2020).
- [15] B. Zhao, D. Khokhriakov, Y. Zhang, H. Fu, B. Karpiak, A. M. Hoque, X. Xu, Y. Jiang, B. Yan, and S. P. Dash, Observation of charge to spin conversion in Weyl semimetal WTe₂ at room temperature, *Physical Review Research* **2**, 013286 (2020).
- [16] A. M. Hoque, D. Khokhriakov, B. Karpiak, and S. P. Dash, Charge-spin conversion in layered semimetal TaTe₂ and spin injection in van der Waals heterostructures, *Physical Review Research* **2**, 033204 (2020).
- [17] Z. Kovács-Krausz, A. M. Hoque, P. Makk, B. Szentpéteri, M. Kocsis, B. Fülöp, M. V. Yakushev, T. V. Kuznetsova, O. E. Tereshchenko, K. A. Kokh, I. Endre Lukács, T. Taniguchi, K. Watanabe, S. P. Dash, and S. Csonka, Electrically controlled spin injection from giant Rashba spin-orbit conductor BiTeBr, *Nano Letters* **20**, 4782 (2020).
- [18] R. Galceran, B. Tian, J. Li, F. Bonell, M. Jamet, C. Vergnaud, A. Marty, J. H. García, J. F. Sierra, M. V. Costache, *et al.*, Control of spin-charge conversion in van der Waals heterostructures, *APL Materials* **9**, 100901 (2021).

- [19] P. Song, C.-H. Hsu, G. Vignale, M. Zhao, J. Liu, Y. Deng, W. Fu, Y. Liu, Y. Zhang, H. Lin, *et al.*, Coexistence of large conventional and planar spin hall effect with long spin diffusion length in a low-symmetry semimetal at room temperature, *Nature Materials* **19**, 292 (2020).
- [20] D. MacNeill, G. Stiehl, M. Guimarães, R. Buhrman, J. Park, and D. Ralph, Control of spin-orbit torques through crystal symmetry in WTe₂/ferromagnet bilayers, *Nature Physics* **13**, 300 (2017).
- [21] M. H. Guimarães, G. M. Stiehl, D. MacNeill, N. D. Reynolds, and D. C. Ralph, Spin-orbit torques in NbSe₂/permalloy bilayers, *Nano Letters* **18**, 1311 (2018).
- [22] S. Shi, S. Liang, Z. Zhu, K. Cai, S. D. Pollard, Y. Wang, J. Wang, Q. Wang, P. He, J. Yu, *et al.*, All-electric magnetization switching and Dzyaloshinskii-Moriya interaction in WTe₂/ferromagnet heterostructures, *Nature Nanotechnology* **14**, 945 (2019).
- [23] Y. Liu and Q. Shao, Two-dimensional materials for energy-efficient spin-orbit torque devices, *ACS Nano* **14**, 9389 (2020).
- [24] J. Hidding and M. H. Guimarães, Spin-orbit torques in transition metal dichalcogenides/ferromagnet heterostructures, *Frontiers in Materials* **7**, 383 (2020).
- [25] G. M. Stiehl, R. Li, V. Gupta, I. El Baggari, S. Jiang, H. Xie, L. F. Kourkoutis, K. F. Mak, J. Shan, R. A. Buhrman, *et al.*, Layer-dependent spin-orbit torques generated by the centrosymmetric transition metal dichalcogenide β -MoTe₂, *Physical Review B* **100**, 184402 (2019).
- [26] M. Vila, C.-H. Hsu, J. H. Garcia, L. A. Benítez, X. Waintal, S. O. Valenzuela, V. M. Pereira, and S. Roche, Low-symmetry topological materials for large charge-to-spin interconversion: The case of transition metal dichalcogenide monolayers, *Physical Review Research* **3**, 043230 (2021).
- [27] C. Safeer, N. Ontoso, J. Ingla-Aynés, F. Herling, V. T. Pham, A. Kurzman, K. Ensslin, A. Chuvilin, I. Robredo, M. G. Vergniory, *et al.*, Large multidirectional spin-to-charge conversion in low-symmetry semimetal MoTe₂ at room temperature, *Nano Letters* **19**, 8758 (2019).
- [28] B. Zhao, B. Karpiak, D. Khokhriakov, A. Johansson, A. M. Hoque, X. Xu, Y. Jiang, I. Mertig, and S. P. Dash, Unconventional Charge-Spin Conversion in Weyl-Semimetal WTe₂, *Advanced Materials* **32**, 2000818 (2020).
- [29] D. Culcer and R. Winkler, Generation of spin currents and spin densities in systems with reduced symmetry, *Physical review letters* **99**, 226601 (2007).
- [30] S. Wimmer, M. Seemann, K. Chadova, D. Koedderitzsch, and H. Ebert, Spin-orbit-induced longitudinal spin-polarized currents in nonmagnetic solids, *Physical Review B* **92**, 041101 (2015).
- [31] M. Seemann, D. Ködderitzsch, S. Wimmer, and H. Ebert, Symmetry-imposed shape of linear response tensors, *Physical Review B* **92**, 155138 (2015).
- [32] A. Roy, M. H. Guimarães, and J. Ślawińska, Unconventional spin hall effects in nonmagnetic solids, *arXiv preprint arXiv:2110.09242* (2021).
- [33] Y. S. Gani, E. J. Walter, and E. Rossi, Proximity-induced spin-orbit splitting in graphene nanoribbons on transition-metal dichalcogenides, *Physical Review B* **101**, 195416 (2020).
- [34] K. S. Novoselov, A. K. Geim, S. V. Morozov, D. Jiang, Y. Zhang, S. V. Dubonos, I. V. Grigorieva, and A. A. Firsov, Electric field effect in atomically thin carbon films, *science* **306**, 666 (2004).
- [35] A. Castellanos-Gomez, M. Buscema, R. Molenaar, V. Singh, L. Janssen, H. S. Van Der Zant, and G. A. Steele, Deterministic transfer of two-dimensional materials by all-dry viscoelastic stamping, *2D Materials* **1**, 011002 (2014).
- [36] G. M. Stiehl, D. MacNeill, N. Sivadas, I. El Baggari, M. H. Guimarães, N. D. Reynolds, L. F. Kourkoutis, C. J. Fennie, R. A. Buhrman, and D. C. Ralph, Current-induced torques with Dresselhaus symmetry due to resistance anisotropy in 2D materials, *ACS Nano* **13**, 2599 (2019).
- [37] E. K. de Vries, A. Kamerbeek, N. Koirala, M. Brahlek, M. Salehi, S. Oh, B. Van Wees, and T. Banerjee, Towards the understanding of the origin of charge-current-induced spin voltage signals in the topological insulator Bi₂Se₃, *Physical Review B* **92**, 201102 (2015).
- [38] P. Li, I. Appelbaum, *et al.*, Interpreting current-induced spin polarization in topological insulator surface states, *Physical Review B* **93**, 220404 (2016).
- [39] E. C. Stoner and E. Wohlfarth, A mechanism of magnetic hysteresis in heterogeneous alloys, *Philosophical Transactions of the Royal Society of London. Series A, Mathematical and Physical Sciences* **240**, 599 (1948).
- [40] C. Safeer, F. Herling, W. Y. Choi, N. Ontoso, J. Ingla-Aynés, L. E. Hueso, and F. Casanova, Reliability of spin-to-charge conversion measurements in graphene-based lateral spin valves, *2D Materials* **9**, 015024 (2021).
- [41] Y. Li and M. Koshino, Twist-angle dependence of the proximity spin-orbit coupling in graphene on transition-metal dichalcogenides, *Physical Review B* **99**, 075438 (2019).
- [42] A. David, P. Rakyta, A. Kormányos, and G. Burkard, Induced spin-orbit coupling in twisted graphene-transition metal dichalcogenide heterobilayers: Twistronics meets spintronics, *Physical Review B* **100**, 085412 (2019).
- [43] T. Naimier, K. Zollner, M. Gmitra, and J. Fabian, Twist-angle dependent proximity induced spin-orbit coupling in graphene/transition metal dichalcogenide heterostructures, *Physical Review B* **104**, 195156 (2021).
- [44] A. Pezo, Z. Zanolli, N. Wittemeier, P. Ordejón, A. Fazzio, S. Roche, and J. H. Garcia, Manipulation of spin transport in graphene/transition metal dichalcogenide heterobilayers upon twisting, *2D Materials* **9**, 015008 (2021).
- [45] N. J. G. Couto, D. Costanzo, S. Engels, D.-K. Ki, K. Watanabe, T. Taniguchi, C. Stampfer, F. Guinea, and A. F. Morpurgo, Random strain fluctuations as dominant disorder source for high-quality on-substrate graphene devices, *Physical Review X* **4**, 041019 (2014).
- [46] C. Neumann, S. Reichardt, P. Venezuela, M. Drögel, L. Banszerus, M. Schmitz, K. Watanabe, T. Taniguchi, F. Mauri, B. Beschoten, *et al.*, Raman spectroscopy as probe of nanometre-scale strain variations in graphene, *Nature Communications* **6**, 1 (2015).
- [47] L. Wang, Y. Gao, B. Wen, Z. Han, T. Taniguchi, K. Watanabe, M. Koshino, J. Hone, and C. R. Dean, Evidence for a fractional fractal quantum hall effect in graphene superlattices, *Science* **350**, 1231 (2015).
- [48] J. H. Garcia, A. W. Cummings, and S. Roche, Spin hall effect and weak antilocalization in graphene/transition metal dichalcogenide heterostructures, *Nano Letters* **17**, 5078 (2017).

- [49] M. Milletari, M. Offidani, A. Ferreira, and R. Raimondi, Covariant conservation laws and the spin hall effect in dirac-rashba systems, *Physical Review Letters* **119**, 246801 (2017).
- [50] J. H. Garcia, M. Vila, A. W. Cummings, and S. Roche, Spin transport in graphene/transition metal dichalcogenide heterostructures, *Chemical Society Reviews* **47**, 3359 (2018).
- [51] J. Ingle-Aynés, F. Herling, J. Fabian, L. E. Hueso, and F. Casanova, Electrical control of valley-zeeman spin-orbit-coupling-induced spin precession at room temperature, *Physical Review Letters* **127**, 047202 (2021).
- [52] D. Bandurin, I. Torre, R. K. Kumar, M. B. Shalom, A. Tomadin, A. Principi, G. Auton, E. Khestanova, K. Novoselov, I. Grigorieva, *et al.*, Negative local resistance caused by viscous electron backflow in graphene, *Science* **351**, 1055 (2016).
- [53] T. Maassen, F. Dejene, M. Guimarães, C. Józsa, and B. Van Wees, Comparison between charge and spin transport in few-layer graphene, *Phys. Rev. B* **83**, 115410 (2011).
- [54] E. McCann and M. Koshino, The electronic properties of bilayer graphene, *Rep. Prog. Phys.* **76**, 056503 (2013).
- [55] T. Maassen, I. J. Vera-Marun, M. H. D. Guimarães, and B. J. Van Wees, Contact-induced spin relaxation in Hanle spin precession measurements, *Phys. Rev. B* **86**, 235408 (2012).
- [56] W. Amamou, Z. Lin, J. van Baren, S. Turkyilmaz, J. Shi, and R. K. Kawakami, Contact induced spin relaxation in graphene spin valves with Al_2O_3 and MgO tunnel barriers, *APL Materials* **4**, 032503 (2016).
- [57] M. Büttiker, Four-terminal phase-coherent conductance, *Physical Review Letters* **57**, 1761 (1986).
- [58] M. Buttiker, Symmetry of electrical conduction, *IBM Journal of Research and Development* **32**, 317 (1988).
- [59] Y. You, Z. Ni, T. Yu, and Z. Shen, Edge chirality determination of graphene by raman spectroscopy, *Applied Physics Letters* **93**, 163112 (2008).
- [60] D. R. Lide, *CRC handbook of chemistry and physics*, Vol. 85 (CRC press, 2004).

Supplementary information of "Omnidirectional spin-to-charge conversion in graphene/NbSe₂ van der Waals heterostructures"

CONTENTS

Introduction	1
Experimental details	2
Results	2
Discussion	4
Summary	6
Acknowledgments	7
References	7
Device fabrication	3
Analysis of the V_{bg} sweeps	4
Measurement of the square resistance of the pristine BLG region	4
Determination of the charge diffusivity	4
Hanle precession at the pristine graphene region	5
Spin-to-charge conversion experiments	7
Reciprocity	8
Spin-to-charge conversion at $V_{bg} = \pm 50$ V	10
Determination of the interface resistance	10
Estimation of the spin Hall angles in NbSe ₂	11
Spin precession with out-of-plane magnetic field in sample 2	12
Determination of the rotation angle between bilayer graphene and NbSe ₂	13
Symmetry considerations	14

DEVICE FABRICATION

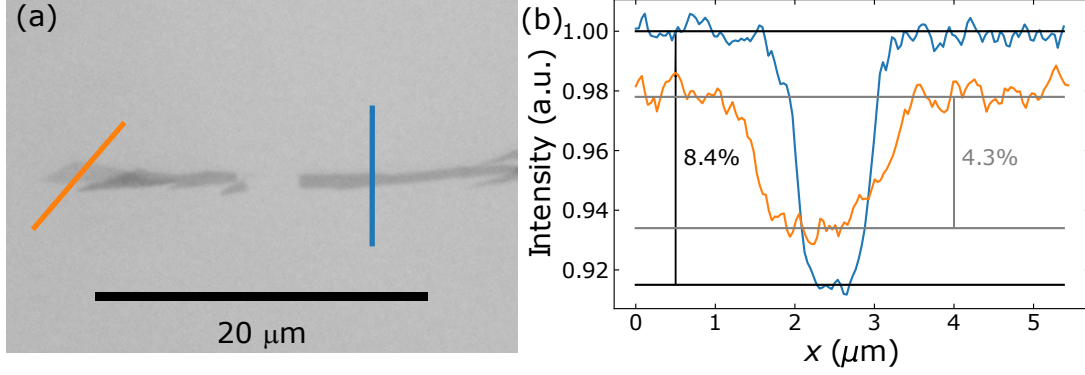


Figure S1. (a) Red channel of the optical microscope image of the bilayer graphene flake used for device 1 (right) and a monolayer graphene region (left). (b) Optical contrast of the monolayer (4.3%) and bilayer (8.4%) graphene flakes. The profiles are taken along the lines in panel a.

The bilayer graphene (BLG) flake was obtained by cleaving a highly oriented pyrolytic graphite crystal (provided by HQ graphene) on a Si substrate with 300 nm of thermal oxide using Nitto tape. To determine the number of layers of the exfoliated flakes, we used optical contrast. Fig. S1 shows that the optical contrast of BLG is twice the one of monolayer graphene.

The NbSe₂ flakes were exfoliated from a bulk NbSe₂ crystal (provided by HQ graphene) on PDMS (Gelpack 4) in a glove box with an Ar atmosphere. The (16-nm-thick) NbSe₂ flake employed in device 1 was transferred on top of the BLG flake shown in Fig. S1a using the viscoelastic stamping technique [35] in the glove box. Next, the Ti (5 nm)/Au (120 nm) contacts were defined using conventional e-beam lithography and deposited by e-beam and thermal evaporation, respectively. To prevent oxidation of the NbSe₂ flake, we minimized the exposure of the flake to air. At this stage, we characterized the NbSe₂ flake by measuring its resistivity (ρ_{NbSe_2}) as a function of T and at different in-plane (B_x), out-of-plane (B_z) magnetic-fields, and backgate voltages (V_{bg}) (Figure S2).

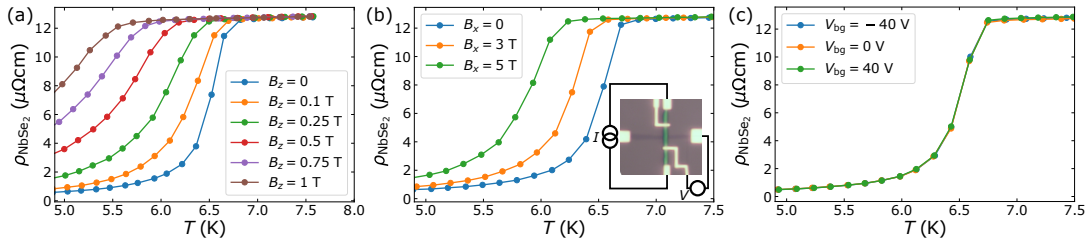


Figure S2. Temperature dependence of the NbSe₂ resistivity for different B_x (a), B_z (b) and V_{bg} (c). The measurement circuit is shown at the inset of panel b.

Finally, the TiO_x/Co electrodes were defined using e-beam lithography and e-beam evaporation of 0.3 nm of Ti, followed by oxidation in air for 10 min, and 35 nm of Co. The ferromagnetic electrodes were capped with 5 nm of Au to prevent oxidation. An optical microscope image of the completed device is shown in Fig. S3.

In total, we prepared 8 devices out of which we could measure spin transport in three of them: The two shown in the report and one where one NbSe₂ arm broke and we could only measure passing a current between the NbSe₂ and graphene flakes. This device showed higher signals, but it is very hard to compare with the others as the measurement geometry is not the same, so we kept it aside. In the 5 remaining devices either the electrical contacts to NbSe₂ were not good enough to measure SCC or the TiO_x/Co contacts were not spin polarized.

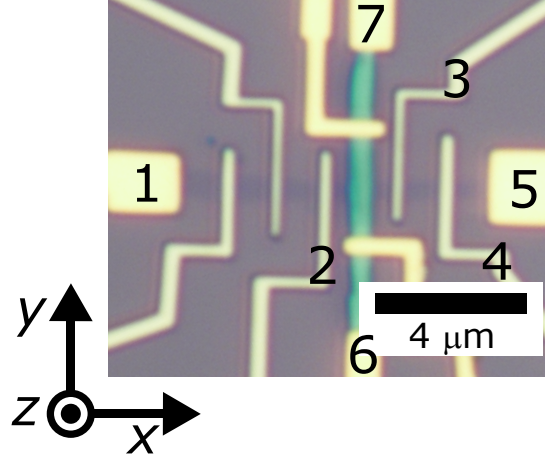


Figure S3. Optical microscope image of the device with the corresponding contact numbering. The grey horizontal stripe is the BLG flake, the green vertical stripe corresponds to the NbSe₂, the vertical contacts to the BLG flake are TiO_x/Co and the other electrodes are Ti/Au.

ANALYSIS OF THE V_{bg} SWEEPS

Measurement of the square resistance of the pristine BLG region

To determine the charge transport properties of the device shown in the main manuscript and Fig. S3, we measured the channel's square resistance (R_{sq}) as a function of the backgate voltage (V_{bg}), that is applied to the doped Si substrate [34]. The V_{bg} controls the carrier density (n) in the graphene channel via the field effect,

$$n = \frac{\epsilon_0 \epsilon_r}{et_{SiO_2}} (V_{bg} - V_{cnp}), \quad (S1)$$

where ϵ_0 is the vacuum dielectric permittivity, $\epsilon_r = 3.9$ is the dielectric constant of SiO₂, e the electron charge, $t_{SiO_2} = 300$ nm is the thickness of the SiO₂ dielectric, and V_{cnp} the value of V_{bg} at which the graphene reaches the charge neutrality point (CNP). In Fig. S4a, we show R_{sq} vs V_{bg} at the pristine graphene region at 300 K obtained by measuring the voltage drop between contacts 3 and 4 (V_{34}) while applying a current between contacts 6 and 5 ($I_{65} = 1$ μ A). R_{sq}^{gr} is determined using

$$R_{sq}^{gr} = (V_{34}/I_{65})(W_{gr}^{34}/L_{34}), \quad (S2)$$

where $W_{gr}^{34} = 1.0$ μ m is the average sample width between contacts 3 and 4 and $L_{34} = 2.0$ μ m is the spacing between contacts 3 and 4 (Table S2). From Fig. S4a, one can observe that R_{sq} shows a clear peak for $V_{bg} = V_{cnp} \approx 7$ V, which corresponds to the CNP, implying that the sample is slightly p -doped at $V_{bg} = 0$ V. At 50 K we see that the position of V_{cnp} has shifted to ≈ 17 V.

Determination of the charge diffusivity

Because of the weak electron-electron interactions in graphene [52], in samples with moderate mobility, the charge (D_c) and spin diffusivity (D_s) can be assumed to be equal [53]. Hence, it is useful to obtain D_c from the V_{bg} sweeps. For this purpose, we use the Einstein relation $D_c = (e^2 R_{sq} \nu(E_F))^{-1}$, where $\nu(E_F)$ is the density of states at the Fermi level. Using the density of states of BLG, the following expression is obtained:

$$D_c = \frac{\pi \hbar^2 v_{f0}^2}{R_{sq} e^2 \sqrt{\gamma_1^2 + 4\pi \hbar^2 v_{f0}^2 |n|}}, \quad (S3)$$

where $v_{f0} = 1 \times 10^6$ m/s is the Fermi velocity of graphene, $\gamma_1 \sim 0.4$ eV is the interlayer coupling parameter between pairs of orbitals on the dimmer sites in BLG [54], and \hbar is the reduced Planck constant. Using Equation S3, the

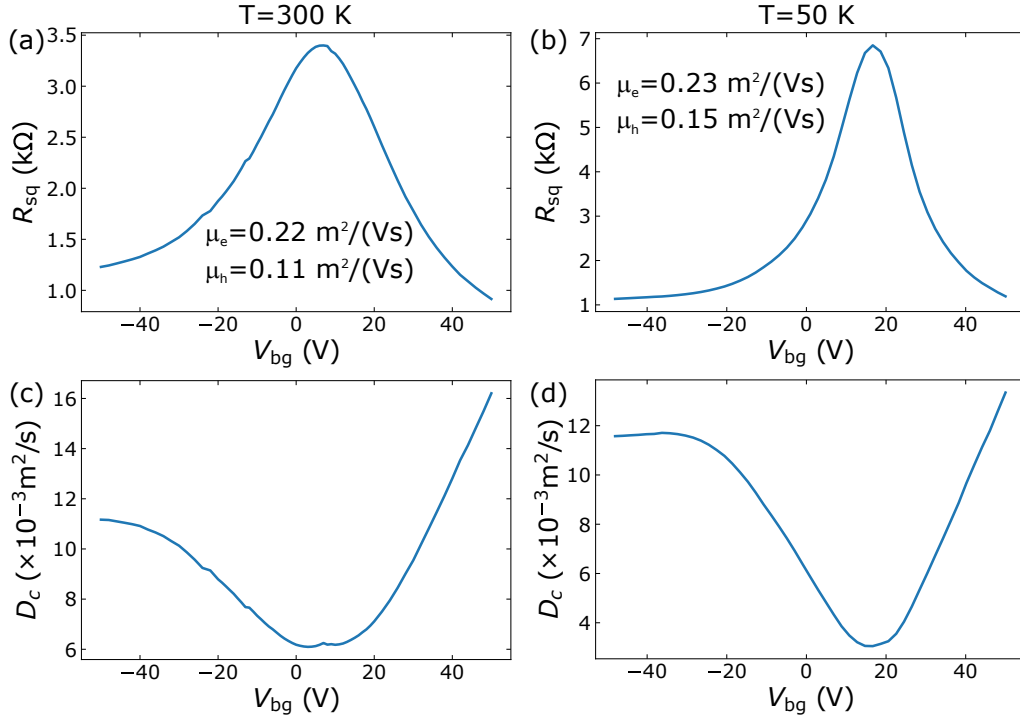


Figure S4. Square resistance $R_{\text{sq}}^{\text{gr}}$ and charge diffusivity D_c^{gr} of the pristine BLG region as a function of V_{bg} at 300 K [panels (a) and (c)] and at 50 K [panels (b) and (d)].

measured R_{sq} , and n (obtained using Equation S1) we obtain D_c^{gr} for the pristine graphene region. These results are shown in Figs. S4c-d. Finally, to determine the charge transport quality of our device, we calculated the field-effect electron (hole) mobility ($\mu_{e(h)}$) using $R_{\text{sq}}^{-1} = ne\mu_{e(h)}$, at $15 \text{ V} < |V_{\text{bg}} - V_{\text{cnp}}| < 40 \text{ V}$. The results are shown in Fig. S4. We observe that the obtained mobilities are of about $2 \text{ m}^2/(\text{Vs})$, as expected for graphene on SiO_2 devices. Additionally, we observe that $1/R_{\text{sq}}$ and D_c are higher at 300 K than at 50 K for all the V_{bg} range except for $V_{\text{bg}} \gtrsim -30 \text{ V}$, where D_c starts to saturate at both temperatures. We attribute this observation to the thermal broadening.

HANLE PRECESSION AT THE PRISTINE GRAPHENE REGION

To extract the spin Hall angle from the measured signals, it is required to obtain the spin transport parameters of the graphene channel. For this purpose, we have performed nonlocal spin transport experiments between contacts 3 and 4 (Fig. S3). As shown in Fig. S5a, by applying a charge current (I) between contacts 3 and 6, a spin current is injected in the graphene channel. The spin current induces a spin accumulation that diffuses in the graphene channel and is detected by measuring the voltage (V) between contacts 4 and 5. When applying a magnetic field along y (B_y) antiparallel to the contact magnetizations (Fig. S5b), the magnetizations of contacts 3 and 4 are switched. Because these electrodes have different coercivities, the switches occur at different B_y values. In this context, measuring the nonlocal resistance ($R_{\text{nl}} = V/I$) as a function of B_y allows the determination of the spin signal in the parallel (R_{nl}^{P}) and antiparallel ($R_{\text{nl}}^{\text{AP}}$) configurations (Fig. S5b). We determine the spin transport properties of the pristine graphene region by performing Hanle spin precession measurements. For this purpose, we apply a magnetic field along x , that induces out-of-plane spin precession (in the $y-z$ plane) before pulling the contact magnetizations along x . In particular, the measured signal in the parallel (antiparallel) configuration can be written as:

$$R_{\text{nl}}^{\text{P(AP)}} = +(-)R_{\text{prec}} \cos^2(\theta_M) + R_0 \sin^2(\theta_M) \quad (\text{S4})$$

Where R_{prec} is the spin precession signal that is the solution of the Bloch equations and includes the spin backflow at the contacts [55], θ_M is the magnetization angle with respect to its easy axis, and $R_0 = R_{\text{prec}}(B_x = 0)$.

The result of measuring R_{nl}^{P} and $R_{\text{nl}}^{\text{AP}}$ vs B_x is shown in Fig. S5c. The spin signal $\Delta R_{\text{nl}} = (R_{\text{nl}}^{\text{P}} - R_{\text{nl}}^{\text{AP}})/2$ is shown

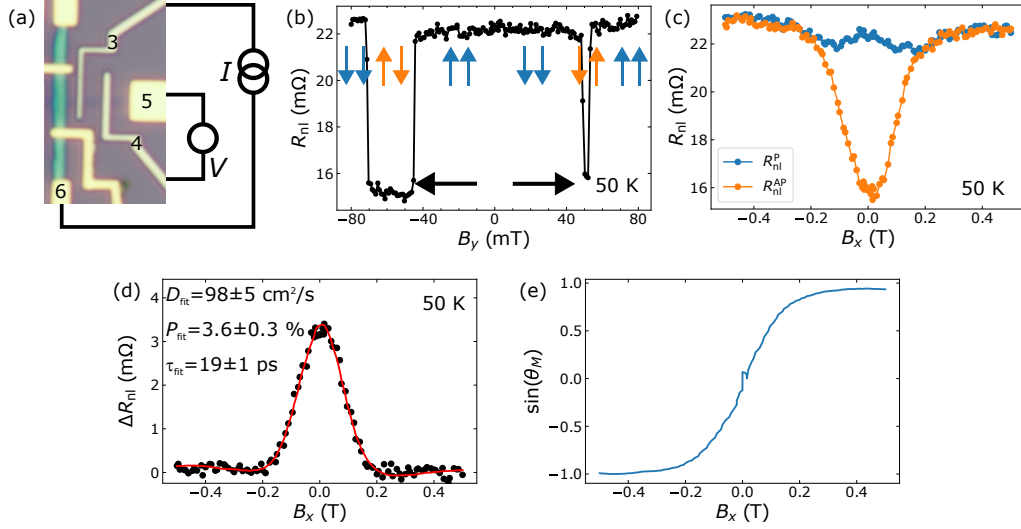


Figure S5. Spin transport in the pristine graphene region. (a) Measurement configuration. (b) Nonlocal resistance as a function of a magnetic field parallel applied along y . The black arrows indicate the B_y sweep direction and the blue and orange arrows indicate the spin injector and detector magnetization configuration obtained assuming that contact 3 switches after 4. (c) Nonlocal resistance as a function of a magnetic field parallel applied along x in the parallel and antiparallel magnetization configurations. (d) ΔR_{nl} vs B_x obtained from panel c, together with its fit to the solution of the Bloch equations and the extracted parameters. (e) B_x -induced pulling of the contact magnetization. The data of panels b-e was obtained at $T = 50$ K and $V_{bg} = 50$ V.

TABLE S1. Spin transport parameters pristine graphene at $V_{bg} = 50$ V.

T (K)	D_{fit} (cm^2/s)	τ_{fit} (ps)	P_{fit} (%)
300	62 ± 7	21 ± 1	5 ± 1
100	109 ± 7	19 ± 1	3.4 ± 0.2
50	98 ± 5	19 ± 1	3.6 ± 0.2

in Fig. S5d, together with its fit to $R_{prec} \cos^2(\theta_M)$, where the contact pulling is obtained using

$$\sin(\theta_M) = \sqrt{\frac{R_{avg} - \min(R_{avg})}{\max(R_{avg}) - \min(R_{avg})}}, \quad (\text{S5})$$

where $R_{avg} = (R_{nl}^P + R_{nl}^{AP})/2$. The result from such an operation is shown in Fig. S5e.

The parameters extracted from the fit are shown in Fig. S5d. We note that the extracted spin lifetime ($\tau_{fit} = 19$ ps) is significantly shorter than typical values obtained in graphene, which are in the 100 ps range. A priori, one could expect that spins are absorbed by the NbSe₂, leading to shorter spin lifetimes in the graphene channel. However, the extracted spin relaxation length ($\lambda_{fit} = \sqrt{\tau_{fit} D_{fit}} \approx 0.4 \mu\text{m}$) is shorter than the distance between contact 3 and the nearest edge of the NbSe₂, which is $1 \mu\text{m}$, implying that the NbSe₂ cannot be the reason for the short λ_{fit} . Because backflow is also included in R_{prec} , and the contact resistances are 9 and 5 k Ω , we conclude that the spin relaxation must occur in the graphene channel. Thus, the most likely reason for the short λ_{fit} is a reduction of the spin lifetime in the graphene channel under the contacts. This effect has been observed in samples with moderate contact resistances where the separation between contacts is short [56]. It is the case in our sample where the contact separation is $1 \mu\text{m}$.

The spin transport measurements in Fig. S5, which are taken at $V_{bg} = 50$ V and $T = 50$ K, have also been performed at other temperatures and the results are shown in Table S1. As it can be seen from there, the results are very similar for the three T values. Even though D_{fit} at 300 K is significantly lower than at 100 and 50 K, we note that it gets compensated by a higher P_{fit} . We attribute this to the fact that D_{fit} is determined by the R_{nl} values at high B_x , which are dominated by contact pulling, the extracted values of D_{fit} may have extra uncertainties.

SPIN-TO-CHARGE CONVERSION EXPERIMENTS

The spin-to-charge (SCC) conversion experiments shown in Figs. 2 and 3 of the main manuscript are performed at temperatures from 3 K up to room temperature and $V_{bg}=50$ V. The raw data, measured in the geometry of Fig. S6a are shown in Fig. S6b-i. At 3 K, the NbSe₂ is superconducting and the signal offset is of about 1 m Ω and R_{nl}^\uparrow is very similar to R_{nl}^\downarrow , which is a bit smaller for $B_x > 0$. Because this signal is comparable to the noise level, we cannot confirm we have SCC in the superconducting regime. At 10 K, the background is lower than 0.2 m Ω and the signal is below the noise level, which is about 0.1 m Ω . For $T \geq 50$ K, R_{nl}^\uparrow and R_{nl}^\downarrow show omnidirectional SCC. In particular, the crossing of R_{nl}^\uparrow and R_{nl}^\downarrow at negative B_x indicates that $R_{SCC} = (R_{nl}^\uparrow - R_{nl}^\downarrow)/2$ contains a symmetric and an antisymmetric component. These features arise from y - and z -SCC (Figs. 1b and 1c of the main manuscript). Additionally, the average between both curves ($R_{avg} = (R_{nl}^\uparrow + R_{nl}^\downarrow)/2$) saturates at a higher value for negative than positive B_x , showing that x -spins are also converted (Fig. 1d of the main manuscript). To quantify the magnitude

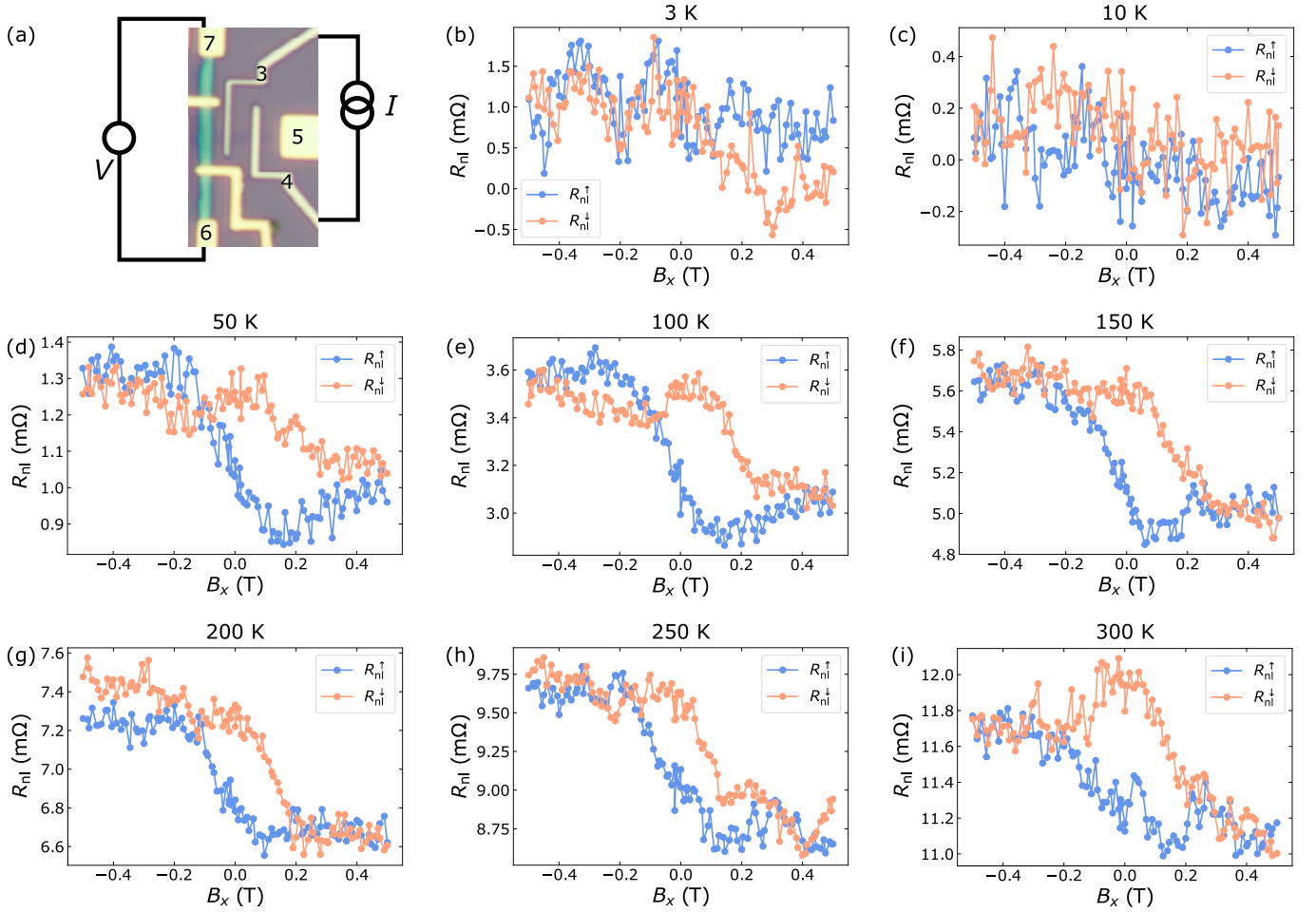


Figure S6. Spin-to-charge conversion measurements at $V_{bg}=50$ V. (a) Measurement configuration. (b-i) Nonlocal SCC signal vs B_x with the spin injector magnetization pointing along $+y \equiv \uparrow$ and $-y \equiv \downarrow$ and for T from 3 to 300 K.

of each SCC component, we have calculated R_{SCC} and R_{avg} . Additionally, to distinguish between the y - and z -SCC components, we have symmetrized (antisymmetrized) the R_{SCC} data and obtained $R_{SCC}^{sym(anti)}$. For this purpose, we have used

$$R_{SCC}^{sym(anti)} = \frac{R_{SCC}(B_x) + (-)R_{SCC}(-B_x)}{2}. \quad (S6)$$

Finally, to compare between the different signals, in Fig. 2 of the main manuscript we define the signal amplitudes ΔR_{avg} , ΔR_{SCC}^{sym} and ΔR_{SCC}^{anti} as the semi-difference between the maximum and minimum signal vs B_x . The result of these operations (Fig. S7a and Fig. 3a of the main manuscript) is that the in-plane SCC components increase with

increasing T , in contrast with the z -SCC component. The B_x -dependent signals are shown for all T in Fig. S7b-i for completeness.

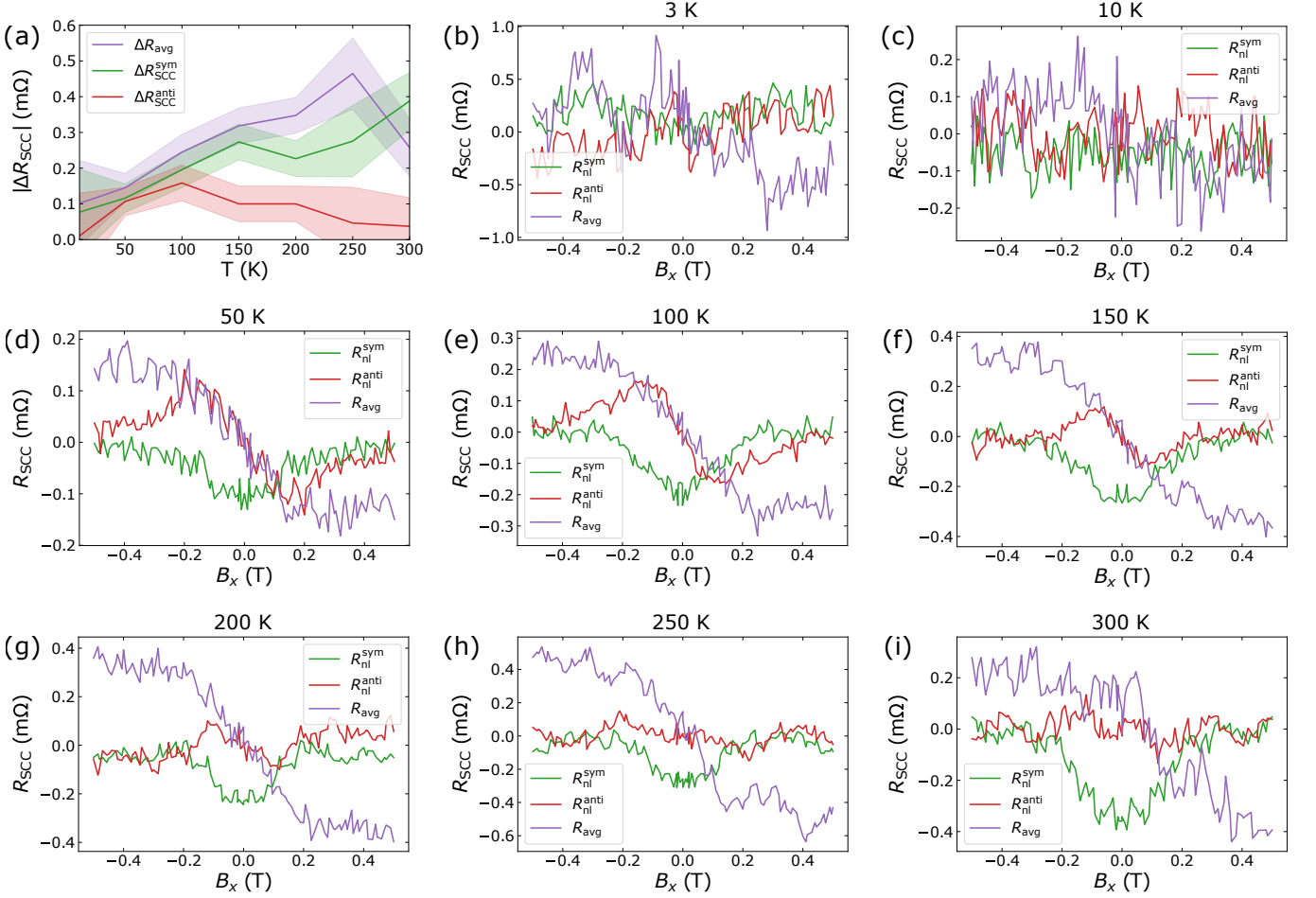


Figure S7. Spin-to-charge conversion components at $V_{bg} = 50$ V extracted from Fig. S6b-i. (a) Maximum signal ($|\Delta R_{SCC}|$) vs T . (b-i) SCC signal as a function of B_x . R_{SCC}^\uparrow and R_{SCC}^\downarrow have been obtained by subtracting R_{nl}^\uparrow from R_{nl}^\downarrow and R_{avg} by averaging. For visualization purposes, an offset has been subtracted from each R_{avg} curve that is determined by its average value.

RECIPROCITY

To confirm that our multiterminal measurements are in the linear response regime, we have measured the reciprocity of our signals comparing $R_{ij,kl}$ with $R_{kl,ij}$, where i, j, k , and l represent the I_+ , I_- , V_+ , and V_- contacts, respectively. The results from such measurement are shown in Figs. S8a and S8b and each SCC component is shown separately in Figs. S8c and S8d. The most important observation is that all the components keep a very similar magnitude. When looking at the signs, we see that the x - and y -SCC components reverse sign between both configurations whereas the z -SCC component does not.

The reciprocity theorem states that [57, 58]

$$R_{ij,kl}(B, M) = R_{kl,ij}(-B, -M), \quad (S7)$$

where $M = \uparrow$ or \downarrow is the contact magnetization. From this expression, one would naively expect that the three SCC components must reverse sign when swapping voltage and current terminals. However, we observe that our data, plotted in Fig. S8, shows that R_{SCC}^{anti} does not change sign. This lack of a sign reversal can be understood by applying Equation S7 to our measurements:

$$R_{nl}^{47,13}(B_x, \uparrow (\downarrow)) = R_{nl}^{13,47}(-B_x, \downarrow (\uparrow)). \quad (S8)$$

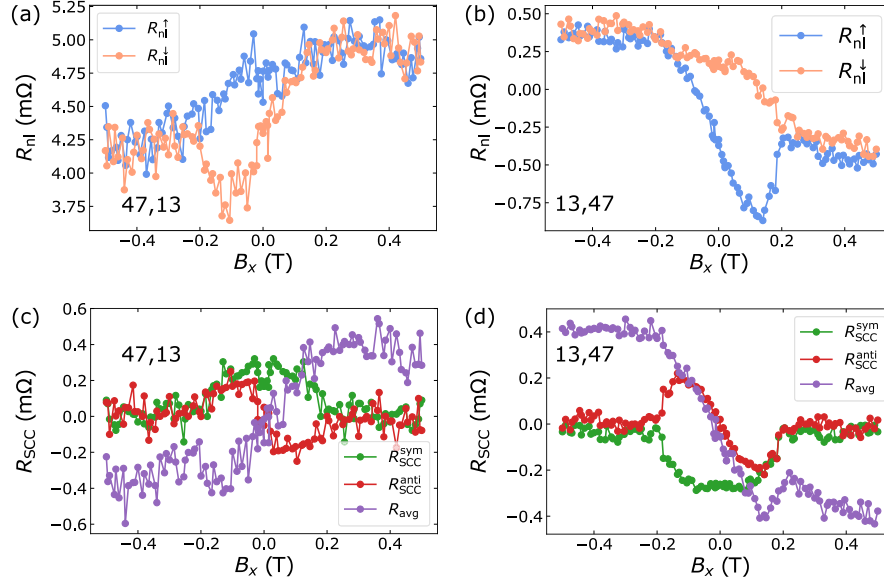


Figure S8. Spin-to-charge conversion [(a) and (b)] and corresponding SCC components [(c) and (d)] in the two reciprocal configurations at 100 K and $V_{bg}=70$ V. In panels (a) and (c), I is applied between contacts 4 and 7 and V measured between 1 and 3. In panels (b) and (d), I is applied between contacts 1 and 3 and V measured between 4 and 7. For visualization purposes, an offset has been subtracted from each R_{avg} curve that is determined by its average value.

We observe that the data in Figs. S8a and S8b agrees well with Equation S8 with the exception of a 4.5 mΩ background which we attribute to the different resistances of the graphene and NbSe₂ arms. To understand how reversing the voltage and current probes affect the different SCC components, we convert Equation S8 into

$$R_{nl}^{47,13}(B_x, \uparrow) - R_{nl}^{47,13}(B_x, \downarrow) = R_{nl}^{13,47}(-B_x, \downarrow) - R_{nl}^{13,47}(-B_x, \uparrow) \quad (S9)$$

by subtracting the two relations Equation S8 contains.

Next, we define $R_{SCC}^{47,13(13,47)}(B_x) = (R_{nl}^{47,13(13,47)}(B_x, \uparrow) - R_{nl}^{47,13(13,47)}(B_x, \downarrow))/2$. Using this definition Equation S9 becomes

$$R_{SCC}^{47,13}(B_x) = -R_{SCC}^{13,47}(-B_x). \quad (S10)$$

The y -SCC component ($R_{SCC}^{47,13sym}$) is symmetric with respect to B_x . This means that it fulfills $R_{SCC}^{47,13sym}(B_x) = R_{SCC}^{47,13sym}(-B_x)$. Combining this expression with Equation S10, we obtain that

$$R_{SCC}^{47,13sym}(B_x) = -R_{SCC}^{13,47sym}(B_x) \quad (S11)$$

and the y -SCC component changes sign.

In contrast, the z -SCC component ($R_{SCC}^{47,13anti}$) is antisymmetric with B_x . This means that $R_{SCC}^{47,13anti}(B_x) = -R_{SCC}^{47,13anti}(-B_x)$ and Equation S10 yields

$$R_{SCC}^{47,13anti}(B_x) = R_{SCC}^{13,47anti}(B_x) \quad (S12)$$

which means that the z -SCC signal does not change sign.

Finally, the x -SCC component does not depend on the initial contact magnetization. To analyze this component separately we have used the following definition: $R_{avg}^{47,13(13,47)}(B_x) = (R_{nl}^{47,13(13,47)}(B_x, \uparrow) + R_{nl}^{47,13(13,47)}(B_x, \downarrow))/2$. Now we use Equation S8 and obtain

$$R_{nl}^{47,13}(B_x, \uparrow) + R_{nl}^{47,13}(B_x, \downarrow) = R_{nl}^{13,47}(-B_x, \downarrow) + R_{nl}^{13,47}(-B_x, \uparrow). \quad (S13)$$

That, using the definition of $R_{avg}^{47,13(13,47)}(B_x)$, turns into:

$$R_{avg}^{47,13}(B_x) = R_{avg}^{13,47}(-B_x). \quad (S14)$$

Because the x -SCC component is antisymmetric with B_x , $R_{\text{avg}}^{47,13}(B_x) = -R_{\text{avg}}^{47,13}(-B_x)$, and Equation S14 leads to

$$R_{\text{avg}}^{47,13}(B_x) = -R_{\text{avg}}^{13,47}(B_x),$$

which implies that the x -SCC component changes sign.

In summary, all SCC components properly fulfill reciprocity, which implies a sign reversal of the y - and x -SCC and no sign reversal of the z -SCC component.

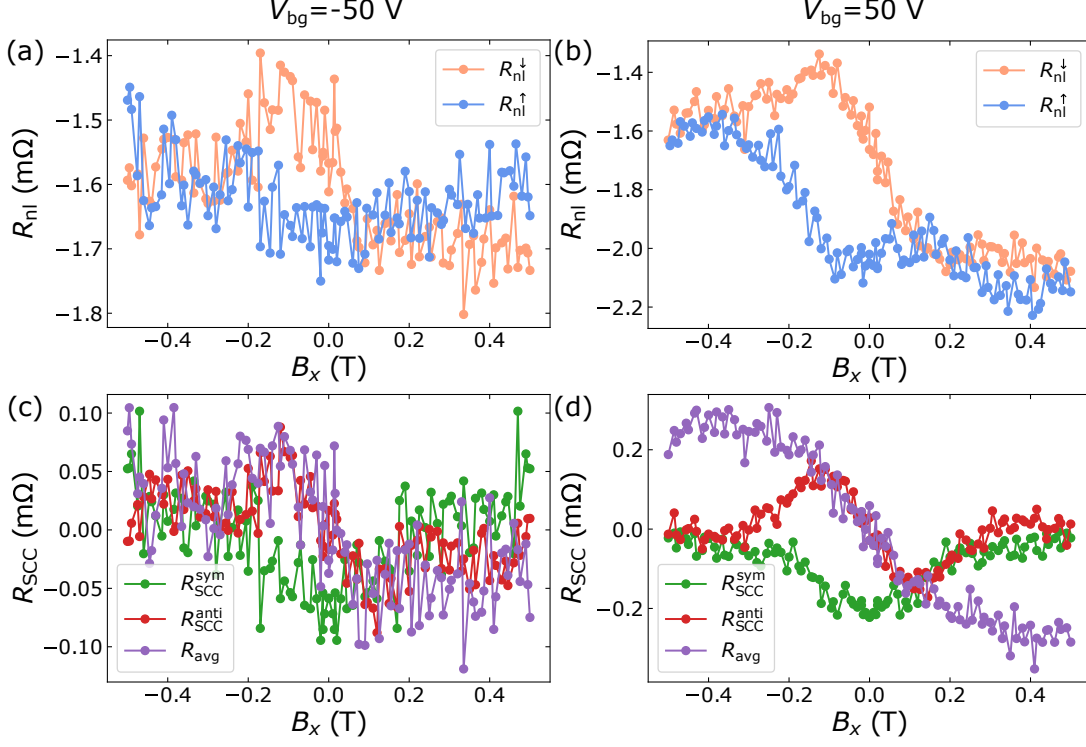


Figure S9. SCC signal as a function of B_x at $T = 100$ K, $V_{\text{bg}} = -50$ V (a) and $V_{\text{bg}} = 50$ V (b). (c) and (d) SCC components extracted from panels a and b, respectively. For visualization purposes, an offset has been subtracted from each R_{avg} curve that is determined by its average value.

SPIN-TO-CHARGE CONVERSION AT $V_{\text{bg}} = \pm 50$ V

Here we show the SCC conversion data obtained at $T = 100$ K and at $V_{\text{bg}} = \pm 50$ V that shines some light on the gate tuneability of the effect. The results are shown in Fig. S9 and demonstrate that omnidirectional SCC is still present at $V_{\text{bg}} = -50$ V, even though its amplitude is significantly smaller than at $V_{\text{bg}} = 50$ V. At $V_{\text{bg}} = 0$ we could not measure any signal below a noise level of 0.5 mΩ.

DETERMINATION OF THE INTERFACE RESISTANCE

To determine the interface resistance (R_{int}) between the bilayer graphene and NbSe₂ flakes, we have used the measurement geometry shown in Fig. S10a. Because R_{int} is smaller than R_{sq} of the graphene channel, the measured resistance (R_{meas}) is negative. Thus, to obtain the correct R_{int} value, we used finite element calculations as in Ref. [27]. The result of such operation is shown in Fig. S10. Because the electrical contacts in sample 1 broke during the measurements due to the large V_{bg} required to measure SCC, we could not obtain its R_{int} at all the measurement temperatures. However, since sample 2 showed a very similar R_{int} at 300 K and R_{int} could be measured for all T values, we have used the low T R_{int} values from sample 2 (red dots in Fig. S10c) to perform the quantitative analysis. Note that, even though the value of R_{meas} is not the same for both samples, the different device dimensions lead to

very similar R_{int} in both cases, in agreement with the fact that both samples were prepared under the same conditions in an inert atmosphere.

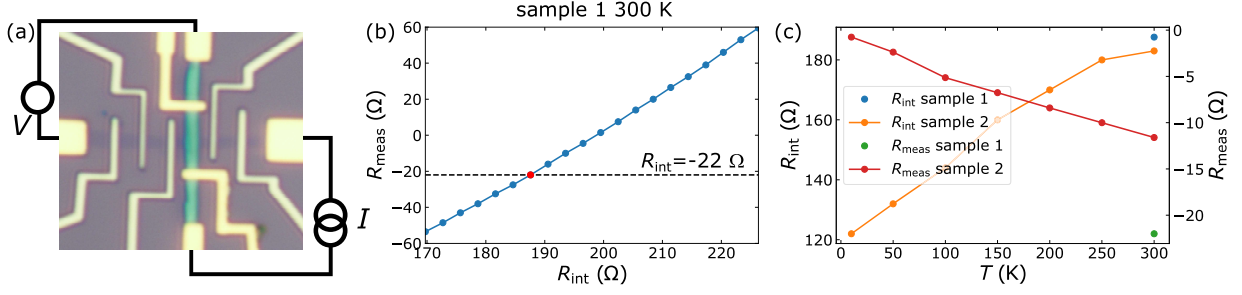


Figure S10. Determination of the interface resistance. (a) Measurement geometry used to obtain $R_{\text{meas}} = V/I$. (b) Relation between R_{int} and R_{meas} from finite element calculations. The intersection between the horizontal dashed line (measured R_{meas}) and the finite-element $R_{\text{meas}}(R_{\text{int}})$, determines the actual R_{int} value (red dot). (c) Summary of R_{int} and R_{meas} of samples 1 and 2 at different temperatures.

ESTIMATION OF THE SPIN HALL ANGLES IN NbSe₂

To determine the spin Hall angles assuming that the SCC occurs in the NbSe₂ flake, we have solved the Bloch equations:

$$D_s \frac{d^2 \vec{\mu}}{dx^2} - \frac{\vec{\mu}}{\tau_s} - \vec{\omega} \times \vec{\mu} = 0 \quad (\text{S15})$$

Here $\vec{\mu} = (\mu_{sx}, \mu_{sy}, \mu_{sz})$ is the spin accumulation, D_s the spin diffusion coefficient and τ_s the spin lifetime. $\vec{\omega} = g\mu_B \vec{B}$ where $\vec{\omega}$ is the Larmor frequency, $g = 2$ the Landé factor, μ_B the Bohr magneton, and $\vec{B} = (B_x, B_y, B_z)$ the applied magnetic field.

The first term in Equation S15 accounts for spin diffusion, the second one for spin relaxation and the last one for spin precession around a magnetic field \vec{B} .

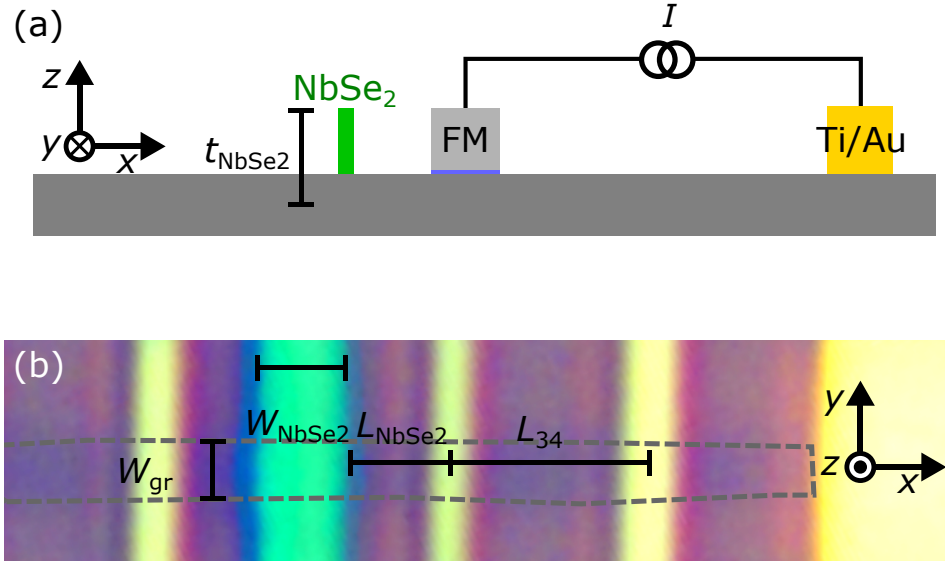


Figure S11. Geometry of the simulated device (a). The BLG (dark grey) is contacted by two ferromagnets (FM) with a tunnel barrier and the NbSe₂ flake (green) that is assumed to be placed at the edge that is closest to the FM spin injector where I is applied. (b) Device image with the relevant dimensions. The BLG edges are indicated as a grey dashed line.

TABLE S2. Geometrical device parameters, contact resistance of the ferromagnetic spin injector (R_c^{FM}), and spin transport parameters used for the θ_{ij}^k quantification summarizing Table S1.

W_{gr}^{34} (μm)	L_{34} (μm)	W_{gr} (μm)	L_{NbSe_2} (μm)	W_{NbSe_2} (μm)	t_{NbSe_2} (nm)	R_c^{FM} (k Ω)	τ_s (ps)	D_s (m ² /s)	P
1.0	2.0	0.80	1.0	0.9	16	6.3	20	0.01	0.035

The modelled geometry is shown in Fig. S11 and takes into account spin precession in the BLG but not in the NbSe₂, which has a much shorter spin lifetime. Backflow at the spin injector is also taken into account [55]. Our model, which is described in detail in Ref. [27], introduces the effect of R_{int} between the BLG and NbSe₂ flakes. The relevant parameters used for the model are shown in Table S2.

To determine the lower bound of the spin Hall angle (θ_{ij}^k), where i , j , and k are the directions of j_s , j_c and s , respectively, we assume that the SCC occurs at the edge of the NbSe₂ that is closer to the spin injector and the width of the NbSe₂-covered region is smaller than the spin diffusion length of the proximitized graphene. Since the spin signal measured across the NbSe₂-covered region is smaller than the noise level, we cannot determine the spin relaxation length of the NbSe₂ ($\lambda_s^{\text{NbSe}_2}$). Therefore, we determine θ_{ij}^k as a function of $\lambda_s^{\text{NbSe}_2}$ (Fig. S12). Since θ_{ij}^k decreases when increasing $\lambda_s^{\text{NbSe}_2}$ until it saturates for $\lambda_s^{\text{NbSe}_2}$ larger than the NbSe₂ thickness, that is 16 nm in our device, we report the lower bound of the θ_{ij}^k [$(\theta_{ij}^k)_{\text{min}}$] obtained assuming $\lambda_s^{\text{NbSe}_2} = 100$ nm. Because we do not know the actual sign of the spin polarization of the Co/TiO_x contacts, we have extracted the absolute value of $(\theta_{ij}^k)_{\text{min}}$ [$(|\theta_{ij}^k|)_{\text{min}}$].

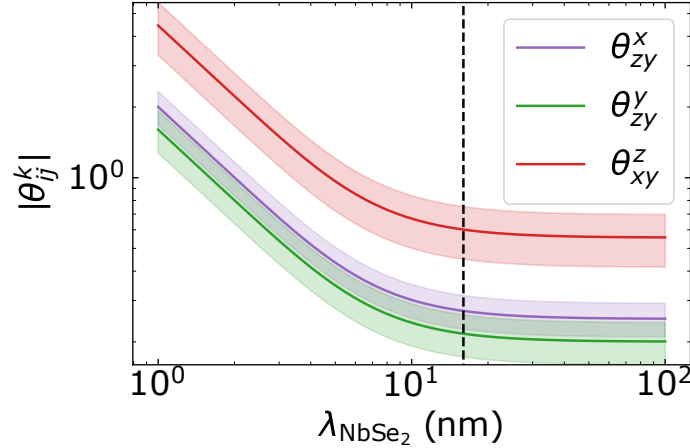


Figure S12. Spin Hall angle as a function of the spin relaxation length in the NbSe₂ flake.

SPIN PRECESSION WITH OUT-OF-PLANE MAGNETIC FIELD IN SAMPLE 2

We have also performed SCC experiments in sample 2. In this case, to demonstrate that the x -SCC component is indeed due to spin transport, we have applied an out-of-plane magnetic field (B_z). B_z induces spin precession in the $x - y$ plane. As a consequence, x -SCC appears as the antisymmetric component in R_{SCC} and y -SCC as the symmetric one. The results from sample 2 are summarized in Fig. S13. There, one can identify both a symmetric and antisymmetric component in R_{SCC} , which show that both x - and y -SCC components are present in sample 2. This observation confirms that the x -SCC component is due to SCC and that both in-plane SCC components are achieved in multiple samples. Another observation we make is that the SCC signal is one order of magnitude smaller than in sample 1, making its observation very challenging. As a consequence, we only observed SCC at 100 K in sample 2. Additionally, for sample 2, we only observed SCC at $V_{\text{bg}} = -50$ and -30 V, in contrast with sample 1, where we observed it at positive V_{bg} . We attribute this observation, that is summarized in Fig. S13b, to a different doping of the BLG flake that gives rise to better spin transport for holes than electrons, in contrast with sample 1.

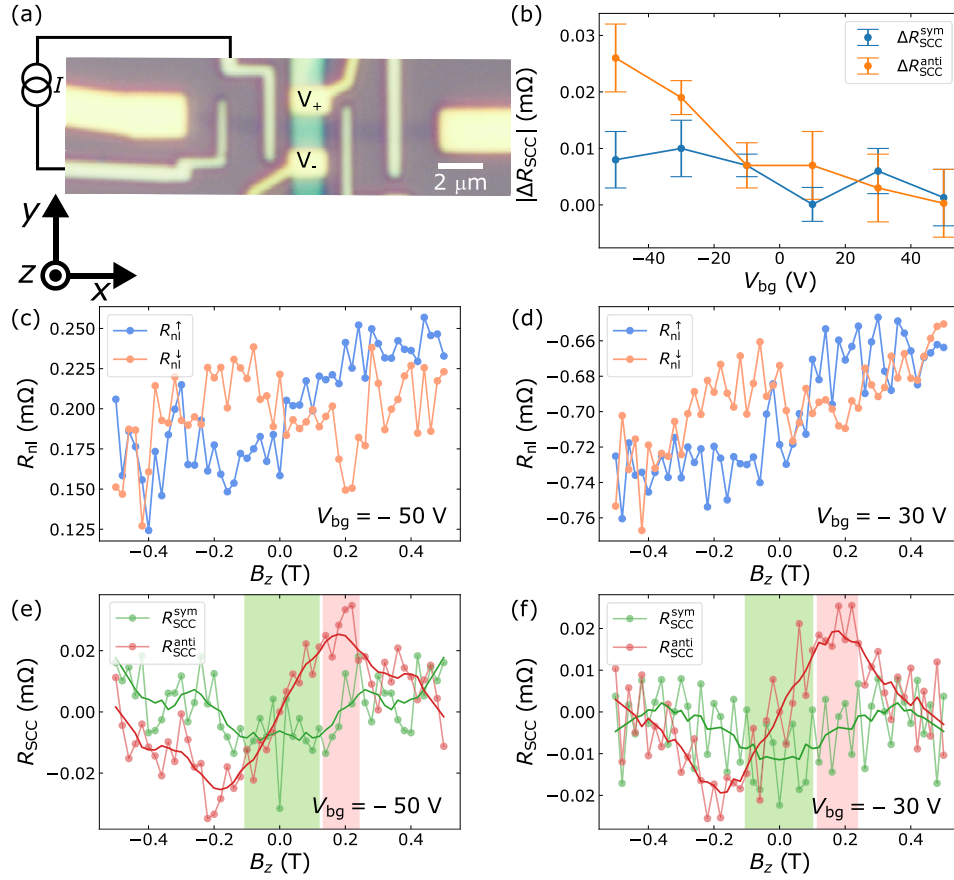


Figure S13. Spin-to-charge conversion as a function of B_z in sample 2 at 100 K. (a) Optical microscope image of sample 2 with the measurement circuit. (b) V_{bg} -dependence of ΔR_{SCC} . (c) and (d) SCC at $V_{\text{bg}} = -50$ and -30 V, respectively. (e) and (f) Symmetric (y -SCC) and antisymmetric (x -SCC) components of $R_{\text{SCC}} = (R_{\text{nl}}^{\uparrow} - R_{\text{nl}}^{\downarrow})/2$ at $V_{\text{bg}} = -50$ and -30 V, respectively. The green and red rectangles highlight the areas that have been used to determine the amplitude and error, that is two standard deviations from the mean for the symmetric and antisymmetric component, respectively. The results are shown in panel b.

DETERMINATION OF THE ROTATION ANGLE BETWEEN BILAYER GRAPHENE AND NBSE₂

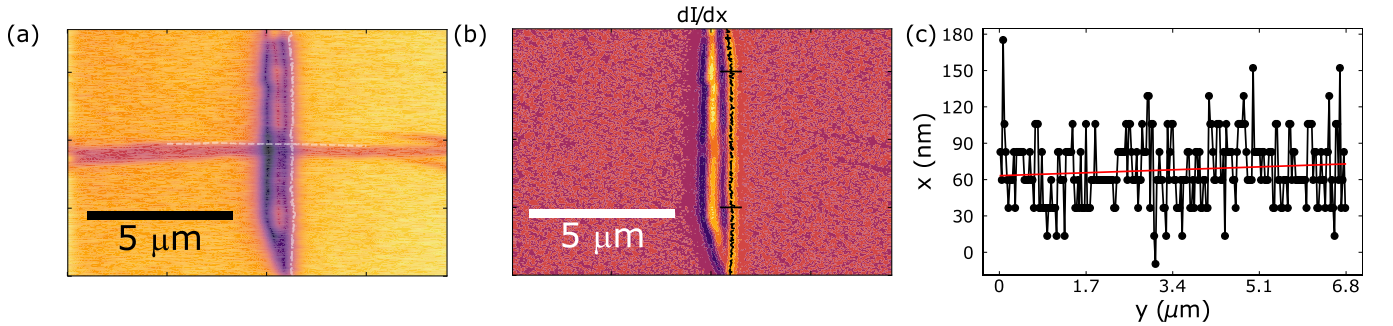


Figure S14. Determination of the flake rotation. (a) Optical microscope image of sample 1 before contact deposition with the estimated edges of the NbSe₂ (vertical) and BLG (horizontal) as dashed lines. (b) Derivative vs x of the intensity of the image in panel a used to determine the edge of the NbSe₂ (dashed line). The horizontal lines limit the range that is used. (c) Linear fit of the points obtained from panel b to obtain the angle between the NbSe₂ edge and the x -axis.

To determine the rotation angle between the BLG and NbSe₂ crystal mirrors, we have assumed that the flakes cleave along a crystallographic axes [59]. In this case, the alignment between the mirrors can be found by analyzing the optical microscope images of sample 1 and finding the rotation angle between the straight edges. To obtain the

edge of the NbSe₂ flake in the most accurate way, we have taken the derivative of the image obtained from averaging the red, green and blue channels of the image (Figs. S14a and S14b) and traced its maximum for each value of y . Next, we have fit the extracted data to a line (Fig. S14c, $x = A + By$ where x is the horizontal and y the vertical coordinate in the image) to obtain its rotation angle with respect to the image using $\tan(\alpha_{\text{NbSe}_2}) = B$. The confidence interval of α_{NbSe_2} has been obtained from the confidence interval of the slope obtained from the fit and assuming that the uncertainty in the determination of the data is its standard deviation from the average value (note that this should lead to a small overestimation due to the small slope of the $x(y)$ line). The result from such analysis is $\alpha_{\text{NbSe}_2} = 89.91^\circ \pm 0.06^\circ$.

To determine the rotation angle of the graphene flake with respect to the image, because its contrast is too small and taking the derivative results in a noisy image, we have determined the edges by visual inspection selecting 7 points that we have plotted as a dashed line in Fig. S14a. From the slope of this line, we have determined the angle of the graphene flake (α_{BLG}), that is $\alpha_{\text{BLG}} = -0.9^\circ \pm 0.6^\circ$. The confidence interval has been obtained assuming that the uncertainty in y is $0.05 \mu\text{m}$ and $\delta\alpha_{\text{BLG}} = \arctan(\sqrt{2} \times 0.05 \mu\text{m} / 6.8 \mu\text{m})$, where $6.8 \mu\text{m}$ is the length of the dashed line. The factor $\sqrt{2}$ comes from the assumption that the uncertainty in the determination of the different points along the edge is not correlated. The value obtained from a linear fit to all the points coincides with the result extracted from the two extreme values.

Finally, the rotation angle between both flakes has been obtained as $\alpha_{\text{NbSe}_2} - \alpha_{\text{BLG}} = 89^\circ \pm 0.6^\circ$.

Similar analysis performed for sample 2 yields a twist angle of $92.7^\circ \pm 0.8^\circ$.

Note that these values are just an estimate and are only valid if the selected edges correspond to crystal mirrors.

SYMMETRY CONSIDERATIONS

Bulk NbSe₂ has space group $P6_3/\text{mmc}$ (194) with corresponding point group $6/\text{mmm}$ (D_{6h}) [60]. Hence, the spin Hall effect (SHE) has only the conventional components, that are given by

$$(J_i)^k = \sigma_{ij}^k E_j \quad (\text{S16})$$

with $i \neq j \neq k$, where $(J_i)^k$ is the spin current density propagating along direction i and polarized along k [29–31]. σ_{ij}^k is the spin Hall conductivity that relates the charge current density E_j along j with the spin current density $(J_i)^k$ via SHE.

In bulk NbSe₂ there is no Edelstein effect (EE) due to inversion symmetry.

Freestanding monolayer NbSe₂ has point group D_{3h} . In this case the SHE still has only conventional components, and the EE is still zero, even though it does not have inversion symmetry.

The surface of bulk NbSe₂ (or monolayer NbSe₂ on a substrate) has point group C_{3v} . The SHE has an extra component $\sigma_{xx}^x = -\sigma_{xy}^y = -\sigma_{yx}^y = -\sigma_{yy}^x$ which is not Hall-like (is symmetric in $i \rightarrow j$) [29–32]. The EE has one term $M_i = \nu_{ij} E_j$ with $\nu_{xy} = -\nu_{yx}$ and the other components are zero. Here, M_i is the induced magnetization, E_j the applied electric field, and ν_{ij} the EE tensor converting the electric field into an induced magnetization. For these components, the mirror in C_{3v} is $x \rightarrow -x$.

The unconventional y -SCC component that we want to characterize has $\vec{j}_c \sim y$ and $\vec{s} \sim y$. This means that the unexpected SCC component can be due to an unconventional EE component (ν_{yy}) or from the SHE component σ_{yz}^y . There is an additional component which is allowed, that is σ_{xy}^y . However, because the signal does not change sign upon reversing the spin diffusion direction along $\pm x$, the latter is not allowed. None of the two possible sources would be allowed even in the less restrictive scenario, that is the surface of bulk NbSe₂, thus, we have to break extra symmetries in our device to explain the measured signal.

Bulk NbSe₂ with shear strain would have broken C_3 , C_{2y} and M_x but preserved M_z and inversion. σ_{yz}^y is allowed in this case, but not ν_{yy} because of inversion symmetry [31].

The surface of NbSe₂ with shear strain has no symmetry left, hence, everything is allowed.

If the mirrors of graphene's symmetry group and NbSe₂ are not aligned, the interface between NbSe₂ and graphene does not have any mirror and ν_{yy} is allowed without the need for shear strain. Where a Nb or Se atom lies on top of a C atom or a hexagon centre this results in a C_3 point group. As explained in the main manuscript, we believe this is the most likely scenario in our devices [41, 42]. In contrast, when the twist angle is 0 or a multiple of 30 degrees, the mirrors are aligned, ν_{yy} is not allowed and, where a Nb or Se atom lies on top of a C atom or a hexagon centre, the heterostructure belongs to the C_{3v} point group.